CHALMERS

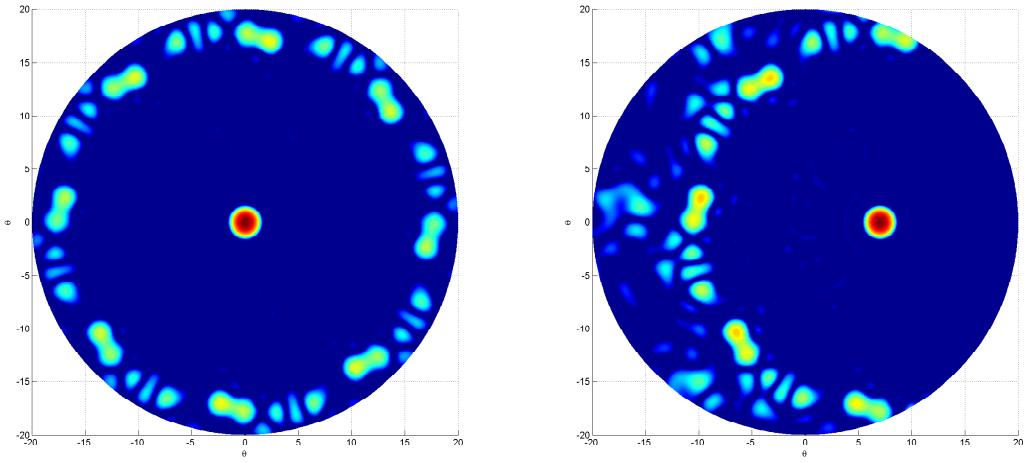

Design Study into Sparse Array Antenna Demonstrators for Future Satellite Systems

Thesis for the Degree of Master of Science

Stellan Johansson

Department of Signals and Systems
Antenna Group
Chalmers University of Technology
Gothenburg, Sweden 2014

Design Study into Sparse Array Antenna Demonstrators for Future Satellite Systems

MASTER's THESIS
as part of mandatory clauses in
fulfillment of Master's Degree from the
Chalmers University of Technology, Gothenburg, Sweden

by

Stellan Johansson
Department of Signals and Systems

October, 2014

Design study into Sparse Array Antenna Demonstrators for Future Satellite Systems / by Stellan Johansson. - Gothenburg : Chalmers University of Technology, 2014.

This thesis is carried out under supervision of:
Dr. Johan Wettergren, Assist. Prof. Dr. Rob Maaskant & Carlo Bencivenni

Examiner:
Assoc. Prof. Dr. Marianna Ivashina

Keywords: sparse array antennas / ℓ_1 norm minimization / satellite communications
Subject headings: future satellite communications / sparse array antennas

Technical Report No. 2014:xx
Antenna Group, Department of Signals & Systems
Chalmers University of Technology,
SE-41296, Gothenburg, Sweden.
Telephone: +46 31 772 1000

Cover design: Broadside and scanned radiation pattern for sparse array antenna.
The work presented in this thesis has been financed by RUAG Space and has been performed at RUAG Space AB as well as Chalmers University of Technology, Sweden.

Abstract

Advances in Direct Radiating Array (DRA) technology have opened up the potential possibility to replace reflector antennas for on-board satellite communication systems by this novel class of antennas. A recently published sparsification algorithm (developed at Chalmers university of technology) is utilized to synthesize cost-effective array configurations that satisfy several stringent constraints imposed by the performance demanding space antenna applications. The research includes the examination of different types of antenna array elements, as well as their impact on the array layouts and construction of an antenna array demonstrator of limited size that serves as a "proof-of-concept" model. The approach for constructing a physical demonstrator that aims at minimizing the number of antenna elements, while accounting for the maximum allowable side-lobe levels under beam-steered conditions ($\pm 8\,^{\circ}$), is discussed. The smallest array candidates utilize in-between 177 and 209 elements in order to realize an illumination spot size of 1°. The larger array candidates employ between 441 and 481 elements in order to realize an illumination spot size of no more than 0.5°. The achieved array sparsification factors are 88–95% and 80–90% for the large and small arrays, respectively. The gains are about 36–39 dBi and 33–36 dBi for the large and small arrays, respectively, with corresponding side lobe levels of about -20 dB and -26 dB from broadside.

Acknowledgments

During the course of this work I have often been in need of support in order make progress. The work presented here would not have been possible without the aid of my supervisors at Chalmers, Carlo Bencivenni and Rob Maaskant. They are very committed and I am grateful for their support. My supervisor at RUAG Space, Johan Wettergren, has also been of great help during the daily work, and I would therefore like to extend my deepest gratitude to him as well.

Contents

List of Figures

Chapter 1

Introduction

In this chapter, the project background and research motivation are provided. A pre-defined set of specifications was provided at the start of the thesis work, which is discussed in detail. Different approaches for a concept design of an antenna is presented, and a brief discussion on the system capacity is provided before outlining the remaining chapters.

1.1 Background and Motivation

The promise of new applications in communication technology has sparked an increased interest in direct radiating array (DRA) technologies during recent years, and several studies in this area have been initiated [1–5]. For onboard satellite communications, DRA:s are widely being considered the successor of reflector antennas [6]. However, applications in the realm of space technology require us to meet challenging specifications, along with heat, vibrations, radiation, weight and power constraints [7]. Reflector antennas are well-suited to cope with these conditions thanks to their robust construction, low weight and high directivity, and as of yet DRA:s are often unsuitable for onboard satellite communication antennas since the large number of required array elements makes the system too heavy and inefficient in terms of power consumption and ohmic losses.

In the light of these facts, the concept of creating sparse array antennas fulfilling well-defined prerequisites is an attractive research topic, possibly enabling DRA:s in future satellite communication systems. This thesis explores the possibility of designing optimal sparse arrays utilizing an in-house developed software. The results are condensed into a suggestion of an array configuration for a transmission band antenna as well as a suggestion to construct a physical demonstrator.

1.2 Initial specification and other prerequisites

At the start of this thesis work, a reference draft specification of the project was provided. In order to determine what type of problems should be considered, the initial specifications, provided below in Table 1.1, will be discussed first. It is pointed out that the specifications are indicative and can be subject to change.

Table 1.1: Initial project specifications.

Frequency band (TX)	17.7-20.2 GHz
Frequency band (RX)	27.5-30.0 GHz
Polarization	RHCP and LHCP
Coverage (circular)	semi-angle 4° (max 8°)
Inter-beam distance	$0.5 - 1°$
Cell system (hexagonal 4 color system)	4 frequency bands in both TX and RX
Edge of Coverage (EOC) gain	To be maximized (beam cross-over is a critical point)
Out of coverage gain, Side Lobe Level (SLL)	>27dB below EOC gain

Frequency bands. The capacity of a wireless transmission link is dependent on the allocated bandwidth. For the given application, the allocated bandwidth is 2.5 GHz for both transmit (TX) and receive (RX). These frequencies are basically located in the K band for TX and Ka band for RX, according to the IEEE standards (the actual limits are 18.0–27.0 GHz for K band and 26.5–40 GHz for Ka band). These bands are traditionally used in radar and satellite communication applications. The TX and RX band separation is due to an absorption peak of water vapor at 22.2 GHz [8]. Each band (TX and RX) will be separated in four different channels, or colors. Each specific spot on the earth's surface will be covered by one channel and the bandwidth for each channel (or color) will be approximately 1 GHz (see last paragraph of this section). The relative bandwidth is low enough not to be considered wide-band, even including both TX and RX bands, but it will probably be more feasible to use separate elements for TX and RX. This would allow for better impedance matching resulting in a more power efficient system architecture.

Coverage, inter-beam distance and color cell system. The specified coverage is circular with a maximum semi-angle of 8°, as to illuminate the whole Earth from geostationary orbit. Indeed, with the Earth radius specified to be 6371 km and assuming a geostationary orbit of 35786 km above earth surface, yields

$$\sin^{-1}\left(\frac{6371}{6371+35786}\right) = 8.69^{\circ}. \tag{1.1}$$

This constitutes an upper limit, and many applications are indeed inclined towards smaller geographical areas. As mentioned before, the coverage will be shaped with the aid of a so-called four color system, i.e., a hexagonal pattern with each adjacent spot assigned a different frequency channel, see Fig. 1.1. From this figure it is also possible to see that the beams will overlap in order to cover the geographical area in a continuous manner, and that the cell cross-over will be the inter-beam distance divided by $\sqrt{3}$.

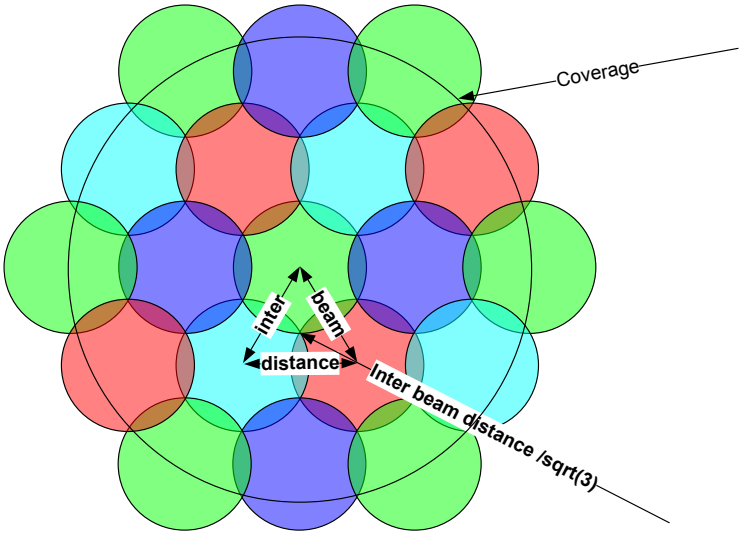

Figure 1.1: Proposed cell color structure for the area of coverage. The inter-beam distance and the cell crossover is illustrated, and the different colors constitute different channels. Note that there is always exactly one beam in-between two beams of the same color.

The inter-beam distance is specified to be between 0.5–1°, which, for a semi-angle of coverage of 8°, will correspond to 16–32 spots over the equator. For symmetry reasons, the number of spots along the diameter needs to be an uneven number, and choosing to illuminate the earth with 15 spots of 1° each over the equator, there would be a need for 169 separate beams for complete earth illumination (see Fig. 1.2 for an illustration of this scenario). Choosing the maximum spatial resolution of 0.5° will increase the number of beams to about 676, possibly placing unrealistic requirements on the on-board hardware requiring an unreasonably large power consumption. It may very well be possible that such a complex system is neither possible nor attractive to realize.

Edge-of-coverage gain and out-of-coverage gain. The color cell system discussed in the above paragraph implies constraints on the radiation pattern. The Edge-Of-Coverage

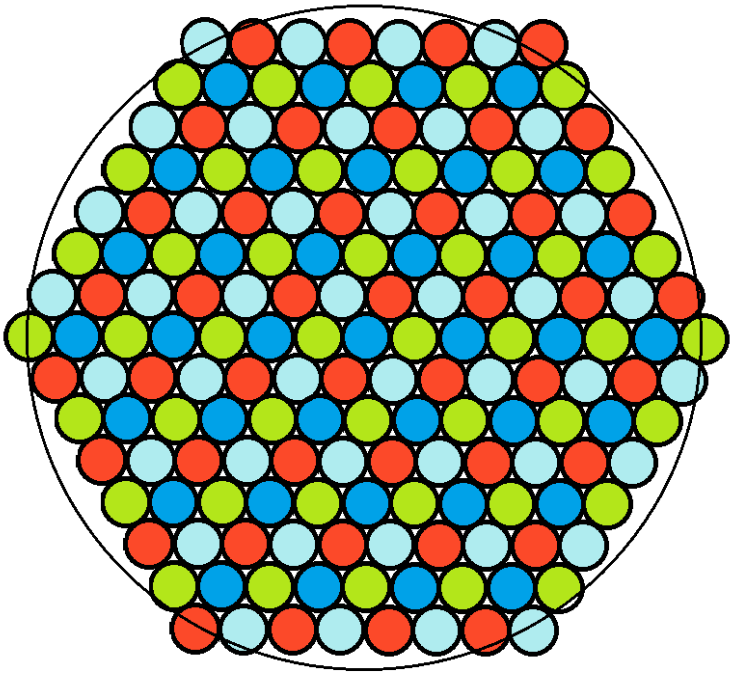

Figure 1.2: For a specified inter-beam distance of 1°, whole-earth coverage consists of approximately 169 separate beams.

(EOC) gain is defined as the gain at the edge of the illuminated spot, and is chosen to be no less than 3 dB below broadside gain. In other words, the signal strength should not drop more than 3 dB inside the illuminated spot. Moreover, the Out-Of-Coverage (OOC) gain, namely the signal level at the closest spot at which the same channel (color) is reused, must be maximum 27 dB below the EOC gain, or 30 dB below the maximum of the main beam level, which is also equal to the maximum Side Lobe Level (SLL) over the Earth's coverage. For inter-beam distances as small as 0.5–1°, this constraint is quite stringent, as it implies a 30 dB drop in signal strength over a scan angle of 0.71–1.42°. Sparse arrays fulfilling constraints of this magnitude have been proposed using an aperiodic pinwheel tiling [2], but the number of elements is still too large to be feasible in a space environment. The algorithm proposed in [1] is used in order to resolve this matter, which is one of the main challenges of this thesis.

The capacity of a future communication system also depends on numerous other parameters which are to be determined by the system engineer. In the following we will perform a brief calculation of this capacity in order to validate the performance of the system. Let us assume that we have separate array elements for both the TX and RX modes so that they can operate independently. For the application at hand it is desired to be power efficient, and for this reason we will use a simple modulation format and a low code rate for the system in order to acquire a more relaxed link budget. Henceforth, we choose the code rate

$R_c = 1/2$ and the spectral efficiency $n = 2$. Coding refers to those methods that introduce redundancy, for example with control bits, while spectral efficiency is the number of bits contained in each transmitted symbol. Furthermore, we utilize two different polarizations and let each channel spacing be 100 MHz including bandwidth edges, i.e., the total amount of channel spacing is 20 % of the total available bandwidth. Thus, the effective bandwidth is 4 GHz in each direction and we obtain a total capacity of 1 Gbit/s for both TX and RX (for each illuminated spot) due to the choice of a hexagonal four color beam system. The interested reader may refer to [9] or similar books to gain a deeper understanding on the subject of capacity.

1.3 Outline

This thesis is organized as follows. Chapter 2 presents some of the theory that is used throughout this thesis. That is, we start by presenting some basic antenna theory where the definition of far-field, co- and cross-polarization as well as directivity are defined. Thereafter, the basic antenna array theory is treated. Starting with a discrete set of array elements, the Fraunhofer approximations are used in order to express the far-field function of an array as an "Array Factor" (AF) multiplied by the far-field function of one of the (identical) array elements. Additionally, the Fourier relationship between an antenna aperture and its far-field function is discussed. Then, the impedance and scattering parameters are defined and in the final section the array antenna synthesis algorithm is discussed.

In chapter 3 the method for synthesizing the array elements and the arrays themselves are presented. The approximate array size is calculated and possible array configurations are shown. The element synthesis and the array synthesis methodology is treated and finally, the approach towards a future physical demonstrator is discussed, and an algorithm used for finding the minimum number of elements for a reduced configuration is presented.

Chapter 4 constitutes the numerical results section, which is subdivided into three parts: the array element simulations and their construction, the full array designs synthesized through the optimization algorithm, and a discussion of the results in the light of different computational aspects as well as the approach to constructing a demonstrator. The element design has resulted in three main candidates: The corrugated pipe horn designed at RUAG Space, and two versions of a pyramidal horn, utilizing different aperture sizes in order to examine the effect of different element gains on the array synthesis. A summary of the array elements is provided. The full array synthesis is presented next. Two separate array aperture sizes, corresponding to two different spot sizes, were considered for each of the three array element types. The chapter also provides recommendations as for which candidates are suitable for construction, and the convergence behavior for these candidates. The last section discusses the previously acquired results.

Chapter 5 provides conclusions drawn from the results and the results discussion. It also contains recommendations for future work.

Chapter 2

Theory

This chapter presents some of the theory that is used throughout this thesis. That is, we start by presenting some basic antenna theory where the definition of far-field, co- and cross-polarization as well as directivity are defined. Thereafter, the basic antenna array theory is treated. Starting with a discrete set of array elements, the Fraunhofer approximations are used in order to express the far-field function of an array as an "Array Factor" (AF) multiplied by the far-field function of one of the (identical) array elements. Additionally, the Fourier relationship between an antenna aperture and its far-field function is discussed. Then, the impedance and scattering parameters are defined and in the final section, the array antenna synthesis algorithm is discussed.

2.1 Basic Antenna Theory

Several antenna theoretical concepts are discussed in the subsequent sections. The notion of near- and far-field is important. Immediately after the electromagnetic energy is transferred from an excited antenna into the surrounding medium it enters the near-field. Little can be said in general about the behavior here, as the propagation is heavily affected by both the antenna geometry and the surrounding environment. There are a few special cases: the point source antenna (which only exists in theory) which exerts spherical wave fronts, and the highly directive antenna, for which the wave fronts are virtually planar directly in front of the aperture. For an antenna of the latter type, aperture diffraction will cause the wave fronts to eventually diverge as they propagate. Most of the energy will be contained within a divergence cone of $2\lambda/L$ radians, where λ is the wavelength and L is the diameter

of the aperture. The effect will be most notable in the far-field, defined in [10] by

$$r \geq \frac{2D^2}{\lambda} \tag{2.1}$$

where r is the radial distance from the antenna, D is the diameter of the smallest sphere containing all structural parts of the antenna, and λ is the wavelength of the transmitted frequency in the surrounding media. The concept of far-field may be used in connection with most antenna types in linear, homogeneous media. There also exists formulas for main beam widths. For instance, the 3 dB main beam width for a circular aperture antenna can be calculated from [8] as

$$\theta_{3\text{ dB}} = 0.886\frac{\lambda}{L} \tag{2.2}$$

and the angular distance between the main beam maximum and the first null can be calculated as

$$\theta_{\text{null}} = 1.226\frac{\lambda}{L}. \tag{2.3}$$

Eq. (2.2) and (2.3) are also valid for a uniformly excited array scanned at broadside.

In the far-field, one typically employs a spherical coordinate system and factors out the dependence on the radial distance from the total E-field according to

$$\mathbf{E}(\mathbf{r}) = \frac{1}{r}e^{-jkr}\mathbf{G}(\hat{\mathbf{r}}). \tag{2.4}$$

In (2.4), the factors are called the divergence factor, the phase factor and the complex far-field function, respectively, and k denotes the wavenumber. Since the waves are propagating in free space they are Transverse Electromagnetic (TEM) and the far-field function will only be a function of the ϕ- and θ coordinates. It is useful to define co- and cross-polar components, where the co-polar component is designated as the desired polarization. If the E-field is linearly y-polarized (i.e. the E-field is oriented along the y-direction) and this is the desired co-polar polarization, we have:

$$\hat{\mathbf{co}} = \hat{\mathbf{y}}, \quad \hat{\mathbf{xp}} = \hat{\mathbf{x}} \tag{2.5}$$

and we define the field components to be[1]

$$E_{\text{co}} = \mathbf{E} \cdot \hat{\mathbf{y}}^* = \mathbf{E}_t \cdot \hat{\mathbf{y}} = E_y \tag{2.6}$$

$$E_{\text{xp}} = \mathbf{E} \cdot \hat{\mathbf{x}}^* = \mathbf{E}_t \cdot \hat{\mathbf{x}} = E_x. \tag{2.7}$$

Correspondingly, if the co-polar polarization is chosen to lie completely in the x-direction, we have that

$$\hat{\mathbf{co}} = \hat{\mathbf{x}}, \quad \hat{\mathbf{xp}} = -\hat{\mathbf{y}} \tag{2.8}$$

[1] * denotes complex conjugation.

and the field components would change accordingly. It is possible to generalize the co- and cross-polar description of any linear polarization using

$$\hat{\mathbf{co}} = \cos\xi\hat{\mathbf{x}} + \sin\xi\hat{\mathbf{y}} \tag{2.9}$$

$$\hat{\mathbf{xp}} = \sin\xi\hat{\mathbf{x}} - \cos\xi\hat{\mathbf{y}} \tag{2.10}$$

and if no specific polarization is required, it is usual to choose ξ in such a way that the cross-polarization is minimized. Thus, the polarization performance of a specific antenna depends on the choice of ξ, or the co- and cross-polar vector alignment.

For any point P contained in the far-field, satisfying Eq. (2.1), the wavefront may locally be approximated as a plane wave. At the observation point P, we can replace the previous coordinate system with the primed coordinate system $\hat{\mathbf{x}}', \hat{\mathbf{y}}'$ and $\hat{\mathbf{z}}'$, so that the field on each point on the far-field sphere may be written as

$$\begin{aligned}\hat{\mathbf{x}}'(\theta,\varphi) &= \cos\varphi\hat{\boldsymbol{\theta}} - \sin\phi\hat{\boldsymbol{\varphi}} \\ \hat{\mathbf{y}}'(\theta,\varphi) &= \sin\varphi\hat{\boldsymbol{\theta}} + \cos\phi\hat{\boldsymbol{\varphi}} \\ \hat{\mathbf{z}}'(\theta,\varphi) &= \hat{\mathbf{r}}.\end{aligned} \tag{2.11}$$

Both the regular and the primed coordinate system is illustrated in Fig. 2.1. From here it is possible to define the co- and cross-polar vectors as

$$\hat{\mathbf{co}} = \hat{\mathbf{y}}'(\theta,\varphi) = \sin\varphi\hat{\boldsymbol{\theta}} + \cos\varphi\hat{\boldsymbol{\varphi}} \tag{2.12}$$

$$\hat{\mathbf{xp}} = \hat{\mathbf{x}}'(\theta,\varphi) = \cos\varphi\hat{\boldsymbol{\theta}} - \sin\varphi\hat{\boldsymbol{\varphi}}. \tag{2.13}$$

This polarization definition is called Ludwig's third definition, or Ludwig III. It is commonly used in antenna theory for high gain antennas.

The maximum available directive gain, or the directivity, is described by the well-known formula

$$D_0 = \frac{4\pi}{\lambda^2}A \tag{2.14}$$

where D_0 is the directivity, λ is the wavelength in the surrounding medium and A is the aperture area. For large antennas ($L > 3\lambda$), however, this is an ideal gain which is practically unattainable due to aperture phase errors, ohmic losses et cetera.

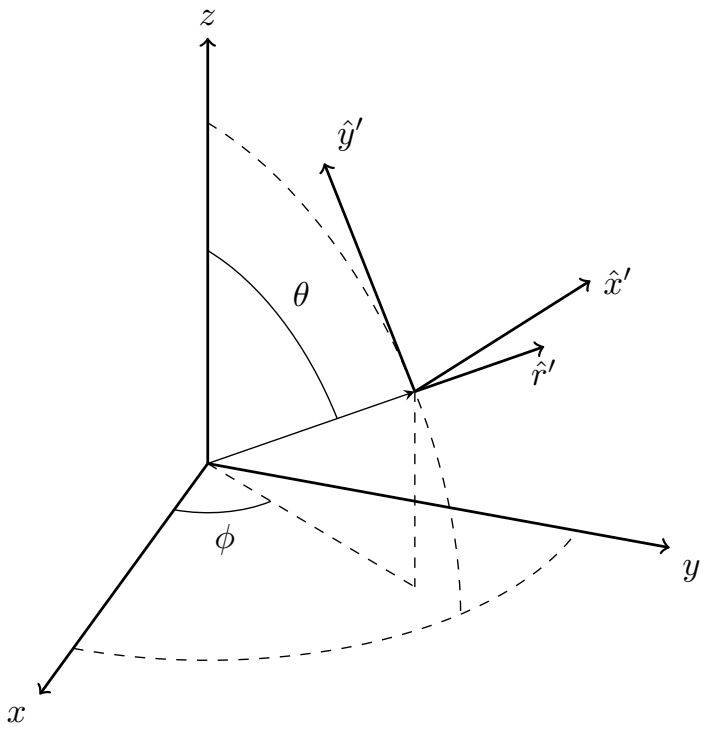

Figure 2.1: Regular and primed coodinate system.

2.2 Array Antenna Theory

There are many different ways of constructing array antennas: microstrip patch antennas, traveling wave slot antennas, resonant array antennas, dipole arrays, et cetera. At this point we will not dwell into the details of how a specific element impacts the system performance, but instead limit our analysis to a generic array antenna built from radiators with control of each elements amplitude and phase weights. We also assume that all observation points are in the far-field if not stated otherwise. The vast amount of literature in antenna array theory starts out with a linear array of equidistant, co-oriented elements with reference points placed according to

$$\mathbf{r}_n = \mathbf{r}_\mathrm{c} + \left(n - \frac{N+1}{2}\right) d\hat{\mathbf{a}} \quad \text{for} \quad n = 1, 2, ..., N \tag{2.15}$$

where $\mathbf{r}_\mathrm{c}$ is the geometrical center of the array, $\hat{\mathbf{a}}$ is the unit vector of the array axis and d is the element spacing. Placing the observation point $\mathbf{r}$ in the far-field allows us to make use of the Fraunhofer approximations. Using the vectors defined in Fig. 2.2 we may state these two approximations as

$$\frac{1}{r} \approx \frac{1}{R} \quad \text{and} \quad r \approx R + \mathbf{r}_n \cdot \hat{\mathbf{r}} \tag{2.16}$$

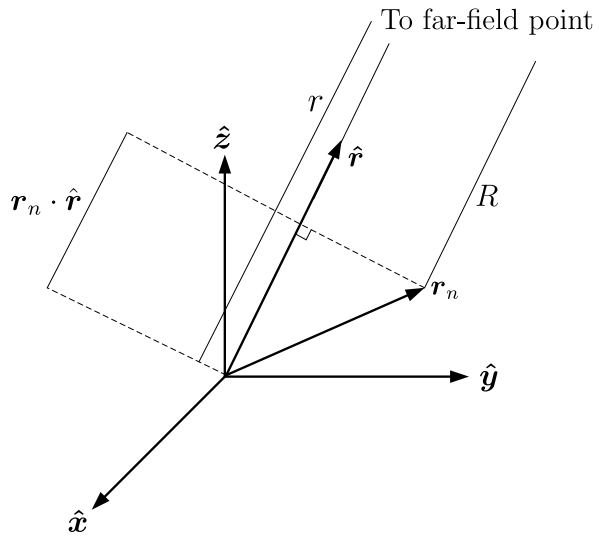

Figure 2.2: Vectors used in connection with the Fraunhofer approximation.

The Fraunhofer approximations state that all rays going from any point of the array to the observation point are assumed to be parallel. They also state that the amplitude difference is assumed negligibly small. This has the implication that if we assume that all elements are identical, the only difference between the radiated far-field for any two array antenna elements is the phase at which the wavefront arrives at the observation point. For the nth element of an array the radiation field at the point $\mathbf{r}$ is written as

$$\mathbf{E}_n(\mathbf{r}) = \frac{1}{r} e^{-jkr} \mathbf{G}(\hat{\mathbf{r}}) e^{jk\mathbf{r}_n \cdot \hat{\mathbf{r}}} \tag{2.17}$$

which is very similar to Eq. (2.4). Here, $\mathbf{G}(\hat{\mathbf{r}})e^{jk\mathbf{r}_n \cdot \hat{\mathbf{r}}}$ is the far-field function when referring it to the global origin of the array antenna multiplied by a phase correction factor. Note the difference between the radiated field at the point $\mathbf{r}$ and the far-field function in the direction $\hat{\mathbf{r}}$: the first is evaluated at a point, the second in a direction. The dependence on radial distance is often dropped as it is regarded as a normalization constant, but this is what links these two vector quantities together. Eq. (2.4) shows this, and the different vectors are illustrated in Fig. 2.2. Using (2.15) and (2.17) we deduct that the far-field

function of the whole array antenna is

$$\mathbf{G}_{\text{Array}}(\hat{\mathbf{r}}) = \mathbf{G}(\hat{\mathbf{r}}) \sum_{n=1}^{N} A_n e^{j\Phi_n} e^{jk\mathbf{r}_n \cdot \hat{\mathbf{r}}} \tag{2.18}$$

where A_n and Φ_n is the amplitude and phase of element number n, respectively, which may be chosen independently; that is, for some direction $\hat{\mathbf{r}}$, the far-field function $\mathbf{G}_{\text{Array}}(\hat{\mathbf{r}})$ for an array antenna is the sum of all the element far-field functions $\mathbf{G}(\hat{\mathbf{r}})$ multiplied with their respective phase difference $e^{jk\mathbf{r}_n \cdot \hat{\mathbf{r}}}$, which is a function of its translation from the array center. The element weights and their relative phase difference due to a spatial separation may be conveniently lumped together to form the so called "Array Factor" (AF) as

$$\text{AF}(\hat{\mathbf{r}}) \equiv \sum_{n=1}^{N} A_n e^{j\Phi_n} e^{jk\mathbf{r}_n \cdot \hat{\mathbf{r}}}, \tag{2.19}$$

so that

$$\mathbf{G}_{\text{Array}}(\hat{\mathbf{r}}) = \mathbf{G}(\hat{\mathbf{r}})\text{AF}(\hat{\mathbf{r}}). \tag{2.20}$$

Eq. (2.20) is intuitive and convenient to use for small N (for large N, however, the calculation time increases and such situations call for other techniques). Owing to the vector format it also applies to irregular (sparse) arrays.

From Eq. (2.19) and (2.20) it is also apparent that the contribution from each element depends only on the amplitude A_n and the phase delay Φ_n of that particular element (assuming all elements are the same). Scanning the beam can be done by setting the element weights as $A_n e^{j\Phi_n} = |A| e^{-jk\mathbf{r}_n \cdot \hat{\mathbf{r}}}$, i.e., in such a way that the phase of the element weights precisely cancels the phase of the array factor in the direction of interest to provide maximum gain. By studying Fig. 2.3 we are made aware that the phase shift in radial direction between two elements placed by the distance d from each other is precisely $d\cos(\theta)$, where θ is the scan angle. Thus, for a linear phased array along x with inter-element distance d and scan angle θ the phase difference between all adjacent elements should be the same, namely

$$\Delta\Phi = -k\mathbf{r}_n \cdot \hat{\mathbf{r}} = -kd\cos(\theta). \tag{2.21}$$

A common inter-element distance is $\lambda/2$, for which the induced phase shift should be

$$\Delta\Phi = -kd\cos(\theta) = -\frac{2\pi}{\lambda}\frac{\lambda}{2}\cos(\theta) = -\pi\cos(\theta). \tag{2.22}$$

Not surprisingly, for broadside scan ($\theta = \pi/2$) the induced phase shift should be zero, and for endfire scan it should be π. Upon choosing the weights in this manner the maximum array gain will be proportional to the number of elements, and the side lobe level will be proportional to one over the number of elements according to

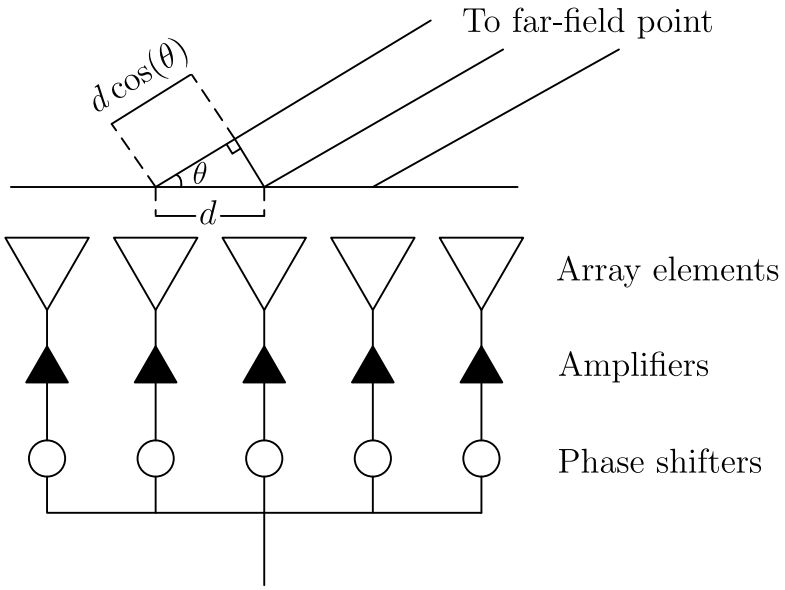

Figure 2.3: Illustration of array scanning.

$$G_{\text{Array}}(\theta) \approx \sum_i G_{\text{element},i}(\theta), \tag{2.23}$$

and

$$\text{SLL}_{\text{power}} \approx \frac{1}{N}. \tag{2.24}$$

2.2.1 Grating Lobes and Fourier Representation of the Far-field

The far-field of an antenna is sometimes described as the Fourier transform of the aperture excitation or field distribution. Hence, uniformly excited apertures of finite extent will be associated with a far-field resembling a sinc-function. Infinite arrays constructed with equidistant elements will have an aperture excitation which will be periodic, and because of this the far-field function of the aperture will also be periodic. This is due to the fact that a periodic function (like a set of equidistant delta spikes, or point sources) has a Fourier transform that is also periodic (another set of delta spikes normalized with a spacing constant), commonly known as a Fourier series expansion. Fourier theory also imply the duality dependence between a signal and its Fourier transform, i.e., smaller element spacings will induce larger angular spacings for the grating lobes in accordance

with the time scaling property of the temporal Fourier transform:

$$f(at) \quad \Leftrightarrow \quad \frac{1}{|a|} F\left(\frac{\omega}{a}\right). \tag{2.25}$$

Another well-known property of the Fourier theory is the frequency shift:

$$f(t)e^{j\omega_0 t} \quad \Leftrightarrow \quad F(\omega - \omega_0). \tag{2.26}$$

Replacing t by Φ and ω by θ, Eq. (2.26) implies that multiplying the weights of an array by a linear phase shift will be the same as shifting the angular spectrum (θ) up or down. This may be observed as scanning the array. Since aperiodic arrays in general do not exhibit periodic grating lobe behavior it is hard to draw general conclusions for any configuration in advance. However, the far-field will still be the Fourier transform of the aperture distribution and scanning the array will thus be executed by employing a linear phase shift.

Visible grating lobes, array scanning, and non-ideal features of the array will degrade the directivity of the antenna. Eq. (2.14) should then be extended to take these effects into account, so that a more realistic directivity can be calculated. This may be done as

$$D = e_{\text{grating}} e_{\text{pol}} e_{\text{ill}} \cos(\theta) D_0 \tag{2.27}$$

where e_{grating} is the grating lobe efficiency, e_{pol} is the polarization efficiency, e_{ill} is the illumination efficiency (which will be assumed to be unity during this thesis work since we only consider plane wave incidence), θ is the scan angle and D_0 is the ideal directivity which is given in Eq. (2.14). Note especially that the available directivity is dependent on θ, since scanning will decrease the effective area of the array.

2.3 Electromagnetic Coupling and Reciprocity

In this section the basic nomenclature for the impedance and scattering matrices are given. For further details on the below-outlined topics, see for instance [10] and [11].

2.3.1 The Impedance Parameters and the Impedance Matrix

The concept of impedance may be defined in several ways. In general, impedance is the quantity describing the relation between voltage and current at a specific point. The role of impedance for an N-port network is similar, as the mutual impedance between port j

and observation port i may be defined as

$$Z_{ij} = \left.\frac{V_i}{I_j}\right|_{I_k=0 \text{ for } k\neq j}. \tag{2.28}$$

This equation defines the impedance at port i with respect to port j as the ratio between the voltage over port i induced by the current flowing into port j. Eq. (2.28) may be modified so that the voltage over port i equals the impedance between ports i and j multiplied with the current flowing into port j. For an N-port system, the total induced voltage at port i is then written as the sum of the impedance of port i with respect to all ports multiplied by the current flowing into all ports. This corresponds to

$$V_i = Z_{i,1}I_1 + Z_{i,2}I_2 + ... + Z_{i,N}I_N, \text{ for } i = 1, 2, ...N \tag{2.29}$$

which in, matrix form, is written as

$$\begin{pmatrix} V_1 \\ V_2 \\ \vdots \\ V_N \end{pmatrix} = \begin{pmatrix} Z_{1,1} & Z_{1,2} & \cdots & Z_{1,N} \\ Z_{2,1} & Z_{2,2} & \cdots & Z_{2,N} \\ \vdots & \vdots & \ddots & \vdots \\ Z_{N,1} & Z_{N,2} & \cdots & Z_{N,N} \end{pmatrix} \begin{pmatrix} I_1 \\ I_2 \\ \vdots \\ I_N \end{pmatrix}.$$

The impedance matrix thus consists of all the mutual impedances between the ports of the system. The self impedances can be seen on the diagonal, and the matrix will typically be symmetric due to reciprocity relations.

2.3.2 The Scattering Parameters and the Scattering Matrix

In microwave networks it is useful to describe the coupling between system ports through so-called scattering parameters. The scattering parameter S_{ij} is defined as the ratio between the voltage wave V_i^- exiting port i to the voltage wave V_j^+ incident to port j, while all ports are terminated in matched loads. This can be written as

$$S_{ij} = \left.\frac{V_i^-}{V_j^+}\right|_{V_k^+=0 \text{ for } k\neq j}. \tag{2.30}$$

Furthermore, the reverse voltage wave exiting port i can be written as the sum of all incident voltage waves going into the network multiplied by the corresponding S-parameter, i.e.,

$$V_i^- = S_{i,1}V_1^+ + S_{i,2}V_2^+ + ... + S_{i,N}V_N^+ \text{ for } i = 1, 2, ...N, \tag{2.31}$$

which, in matrix form, is written as

$$\begin{pmatrix} V_1^- \\ V_2^- \\ \vdots \\ V_N^- \end{pmatrix} = \begin{pmatrix} S_{1,1} & S_{1,2} & \cdots & S_{1,N} \\ S_{2,1} & S_{2,2} & \cdots & S_{2,N} \\ \vdots & \vdots & \ddots & \vdots \\ S_{N,1} & S_{N,2} & \cdots & S_{N,N} \end{pmatrix} \begin{pmatrix} V_1^+ \\ V_2^+ \\ \vdots \\ V_N^+ \end{pmatrix}.$$

Both the impedance matrix and the scattering matrix provide full information about the signal and noise interaction at the ports of the network, and it is possible to convert one characterization into another. The relations between the scattering and impedance matrices $\mathbf{S}$ and $\mathbf{Z}$ are

$$\mathbf{S} = (\mathbf{Z} + \mathbf{U})^{-1}(\mathbf{Z} - \mathbf{U}) \iff \mathbf{Z} = (\mathbf{U} + \mathbf{S})(\mathbf{U} - \mathbf{S})^{-1} \tag{2.32}$$

where $\mathbf{U}$ is the identity matrix.

2.4 Numerical Optimization of the Sparse Irregular Array

The traditional approach to sparse array synthesis is to minimize the number of array antenna elements. This can be referred to as minimizing the ℓ_0-norm (i.e. the number of non-zero elements) of the solution, which is a non-convex optimization problem and thus difficult to solve. The algorithm used here solves the same problem in a semi-analytical manner by minimizing the ℓ_1-norm (i.e. the euclidian lengths of the element weights) in an iterative fashion, which has proven to converge quickly and yield very good results [1]. Assume N elements are placed at arbitrary positions $\{\mathbf{r}_n\}_{n=1}^N$ and let $\{\boldsymbol{f}_n\}_{n=1}^N$ be the corresponding set of embedded far-field vector element patterns. The far-field function can then be written as

$$\boldsymbol{f}(\hat{\mathbf{r}}) = \sum_{n=1}^{N} w_n \boldsymbol{f}_n(\hat{\mathbf{r}}) \quad \text{where} \quad \boldsymbol{f}_n(\hat{\mathbf{r}}) = \boldsymbol{f}_n^0(\hat{\mathbf{r}}) e^{jk\mathbf{r}_n \cdot \hat{\mathbf{r}}}. \tag{2.33}$$

Note that $\boldsymbol{f}_n$ takes into account the propagation phase delay with respect to $\boldsymbol{f}_n^0$, which is the element index whose coordinates are used as the phase reference point. The weight w_n is the nth element in the complex excitation vector $\mathbf{w}_n = [w_1, w_2, ..., w_N]^T$. This is the weight vector that should be minimized in an ℓ_0-norm sense. In accordance with [1], the problem can be solved approximately through an iterative ℓ_1-norm minimization algorithm as

$$\underset{\mathbf{w}\in\mathbb{C}^N}{\operatorname{argmin}} ||\mathbf{Z}^i \mathbf{w}^i||_{\ell_1}, \quad \text{subject to} \quad \begin{cases} f_\nu(\hat{\mathbf{r}}_s) = 1, \\ |f_\nu(\hat{\mathbf{r}})|^2 \leq M(\hat{\mathbf{r}}), \hat{\mathbf{r}} \in \text{mask} \end{cases}$$

where ν belongs to {co,xp} and thus denotes the component of the far-field to consider. The scalar function $M(\hat{\mathbf{r}})$ is the side lobe level mask taken into account during the iterative minimization, where i is the iteration count. The matrix $\mathbf{Z}^i$ is a diagonal matrix with elements given as $z_p^i = 1/(|w_p^{(i-1)}| + \epsilon)$, which helps to make the solution sparser during the minimization. That is, redundant elements are suppressed through the magnification of their contribution to the minimization by an amount based on previous iterations. The parameter ϵ is set slightly smaller than the expected active weights in order to provide the

fastest possible convergence. It also enables elements which have been turned off to be turned back on.

Instead of solving the problem for the embedded patterns directly, the algorithm is composed of two steps (see Fig. 2.4). During the initialization phase, the algorithm employs a finely sampled element placement grid with a resolution of typically a fraction of a wavelength. This grid is used to synthesize a maximally sparse array in the absence of electromagnetic coupling effects. Instead, phase-corrected versions of an electromagnetic-simulated isolated element pattern are assumed. An initial optimal solution of the problem is acquired by performing iterative ℓ_1-minimization until convergence is reached. Elements are considered active if their excitation weights exceed a certain threshold.

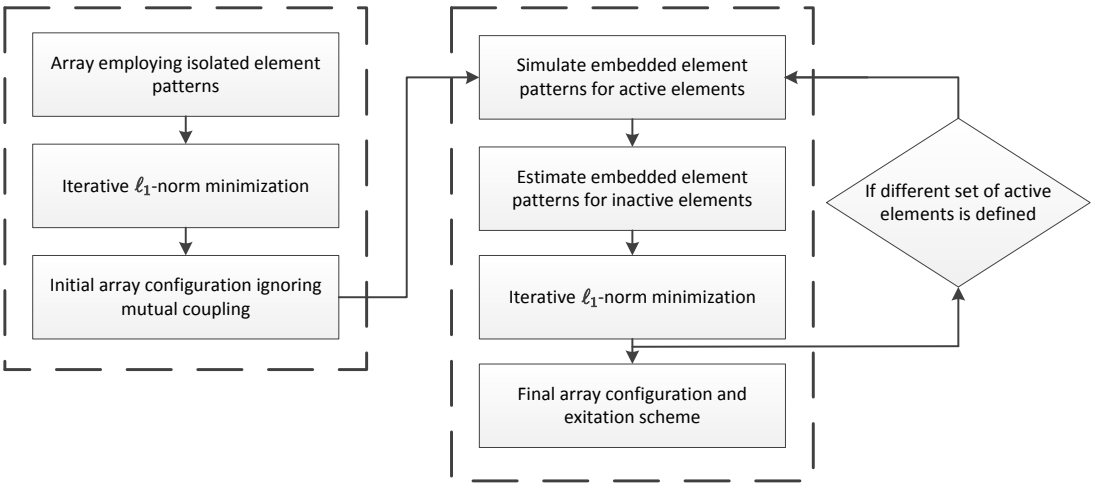

Figure 2.4: Flowchart describing the operating principle of the algorithm. Note how the algorithm employs both isolated and embedded element patterns in conjunction with the iterative ℓ_1-norm minimization.

The EM coupling effects are introduced during the second phase with the aid of a full-wave analysis where only the active elements of the solution acquired in the previous step are retained. This is done to replace the isolated element patterns by their embedded element patterns. The patterns of the inactive elements are estimated by assuming a phase corrected version of the nearest active embedded element pattern. This way it is possible to assume embedded patterns for all element positions, and so, it is possible to further optimize the element configuration under embedded pattern conditions.

Chapter 3

Method for Element and Array Synthesis

In this chapter the method for synthesizing the array elements and the arrays themselves are presented. The approximate array size is calculated and possible array configurations are shown. The element synthesis and the array synthesis methodology is commented and finally, the approach towards a future physical demonstrator is discussed, and an algorithm used for finding the minimum number of elements for constructing a demonstrator is presented.

3.1 General Approach

With reference to Eq. (2.2), the beam width is directly proportional to the wavelength and inversely proportional to the aperture size of a regular directive antenna. The same is valid for an array antenna where the aperture of the array can be thought of as the total antenna size. A required inter-beam distance of 0.5–1 ° and a wavelength of 16.9 mm (corresponding to the lowest specified operating frequency of 17.7 GHz) requires an aperture size of

$$L = 0.886\frac{\lambda}{\theta_{3\,dB}} \;\Rightarrow\; 0.86\,\mathrm{m} \leq L \leq 1.72\,\mathrm{m} \tag{3.1}$$

which corresponds to the regime of the reflector antennas that are employed today. It is a reasonable assumption that the synthesized array needs to be of approximately this size in order to fulfill the beam specifications; that is, the farthest distance between any two array elements should be in the order of 0.86–1.72 m, depending on the desired beam

width. This is equivalent to 50.7–101.4 λ (86–172 λ for the highest specified frequency), and is thus an example of the large electrical size of these problems and the reason advanced computational algorithms are needed.

Depending on the final configuration of the array elements, several antenna concepts are possible to consider, as e.g. depicted in Fig. 3.1. Other candidates might be possible too, but the discussion is limited to these cases since the treatment of them is sufficient in order to discuss the main questions and figures of merit that will be important during the construction of sparse antenna arrays. The three different cases are:

(a) Separate TX/RX apertures with separate TX/RX element designs. This approach utilizes separate TX and RX antennas. It permits each of the antennas to be constructed independently and will reduce EM coupling between the elements in TX and RX. Also, the use of separately developed antenna elements will allow for good matching to the signal network. However, the construction suffers from the risk of ending up with array solutions that are too heavy and impractical for satellite communication purposes.

(b) Combined TX/RX aperture with separate TX/RX element designs. Here, the TX and RX antennas share the same aperture but utilize different types of antenna elements. This allows for a compact design and good matching, but the elements will be located closer to one another than in Case (a) and will for this reason be subject to higher EM coupling, even if the elements are designed for separate frequency bands and will couple less for this reason. Furthermore, it will be impossible to realize if the element configuration is too dense. One possible solution to a too dense element configuration is to enlarge the allowed aperture size which should lead to a more sparse configuration. However, if the total weight and size of the antenna gets close to (or exceeds) that of Case (a) one might as well choose Case (a) in order to acquire better isolation between TX and RX channels.

(c) Combined TX/RX aperture with combined TX/RX element design. The last approach utilizes the all-in-one approach, the TX and RX channels share the same aperture and antenna elements. This has the major drawback that the capacity will be one half of the previous cases. This is because the TX and RX channels will share the same feeds with a transceiver for switching between TX and RX modes. It will also be subject to higher EM coupling, so that the elements will be designed as a compromise between the TX and RX band. This suboptimal element design will lead to degraded impedance matching. However, the design is compact and cheap to fabricate due to the fact that only one element type will be needed. The element configuration can also be chosen freely as in Case (a).

The final choice of array configuration will depend on the results yielded both by the choice of the array elements as well as the element array configuration as determined by the minimization algorithm. Initially, several options are possible. In the following we discuss the method for acquiring the array element and its layout.

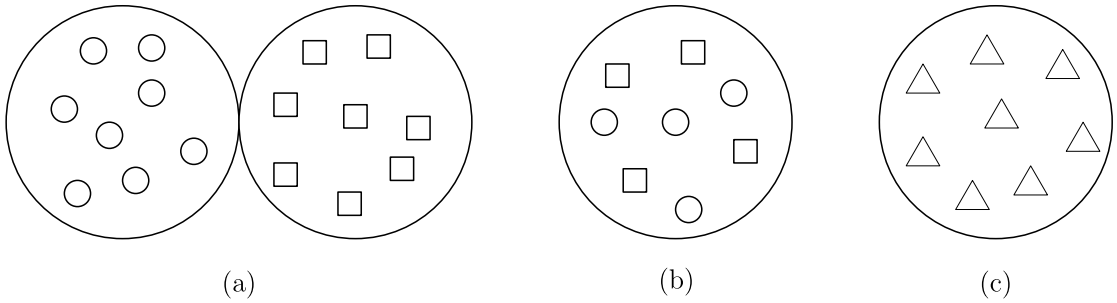

Figure 3.1: Different concepts for realizing sparse array antennas. (a) Separate TX/RX apertures with separate TX/RX element designs. (b) Combined TX/RX aperture with separate TX/RX element designs. (c) Combined TX/RX aperture with combined TX/RX element designs.

3.2 Antenna Array Element Construction

Since the design problem at hand is intended for geostationary satellite communication applications, we may assume whole-earth coverage and thus assume a maximum scan angle of $\pm 8.69^\circ$ as calculated in (1.1). It is desired to focus the radiated energy within the Area Of Coverage (AOC) both for lowering the power consumption and to lower the receiver noise. In fact, the latter effectively lowers the power consumption since it provides increased SNR and will enable a more relaxed link budget. Even though the average background noise temperature of free space is as low as about 4 K, the sun could possibly increase the noise temperature of the system, which is also a reason to minimize the gain outside the AOC.

We know from Eq. (2.17) that the radiated field at a point $\mathbf{r}$ is proportional to the far-field function in the direction pointing towards $\mathbf{r}$. This dependence is also valid for an array, as the radiated far-field of an array is simply the far-field function of a single element multiplied by the array factor AF, in accordance with (2.20). This is correct for any finite array configuration under the assumption that no mutual coupling occurs, which for a real array is not the case. However, the overall behavior is qualitatively still the same. For this reason, the elements may not have a main beam narrower than the AOC since this will impinge negatively on the possibility for the array to provide whole-earth coverage. Elements that are too large will also lower the flexibility of placement during the array synthesis process; smaller elements may be placed closer to one another without colliding. In conclusion, the optimal array element would be as small as possible providing maximum gain, i.e., flat gain over the specified AOC and zero outside. Elements with these properties

are of course impossible to realize physically and presents a trade-off between element size, gain flatness over the AOC and element directivity.

In an actual implementation of the system the signal pathway leading up to the elements would likely be waveguides as they exhibit superior power efficiency. Simulating arrays using wave ports in the CAD software FEKO, however, is not possible. This is because the current version of the FEKO software lacks the required functionality. A workaround to this problem is to construct a monopole at the transition that is excited by a voltage port. This has also been done in the CAESAR software [12]. However, this has implications on the gain pattern, which becomes somewhat asymmetrical due to the onset of higher order modes in the waveguide section. Employing asymmetrical patterns in the minimization algorithm could possibly prohibit convergence to a feasible solution. The distance from the monopole to the horn section was increased in order to obtain more symmetrical gain patterns, that is, through extending the waveguide section so that evanescent modes would sufficiently decay before entering the element aperture. This is the reason for the long waveguide section in Fig. 3.2 that for the element simulations is attached to the horn part of the element. The implications of this can be seen in Fig. 3.3, where different gain patterns have been plotted for different waveguide lengths. The pattern is observed from broadside direction, $\theta = 0$, and the monopole is mounted on the far right wall in the $\varphi = 0$ plane. The radiated power is a function of φ; In fact, the pattern varies heavily with both θ and φ. The θ dependence is desired since the antenna pattern should taper off quickly outside of AOC, but the variation in φ complicates the scanning since the far-field function will be different for different φ cuts. As the feeding waveguide separating the monopole and the flare gets longer, the pattern becomes more symmetrical, which is a highly desirable property from a pattern synthesis point of view.

3.2.1 Independent Optimization of Feed and Horn

To construct the antenna element such that it is well-matched and provides sufficiently large gain, the geometry is split between a transition, or feed, and a horn part (see Fig. 3.2). The proposed approach is to optimize these sections separately and merge them later on. The aperture at which the element is split is terminated by a wave port in order to simulate a perfectly impedance-matched interface. This allows for designing several different candidates; it is for instance possible to optimize the horn for a different flare length without compromising the element input impedance matching. As both parts could be analyzed separately, it is possible to design well-matched element candidates with different gains, which can then be used in the array optimization process.

(a) (b)

Figure 3.2: The different parts of the horn. (a) The bottom feeding part, including the voltage pin excitation. (b) The top, or horn antenna part.

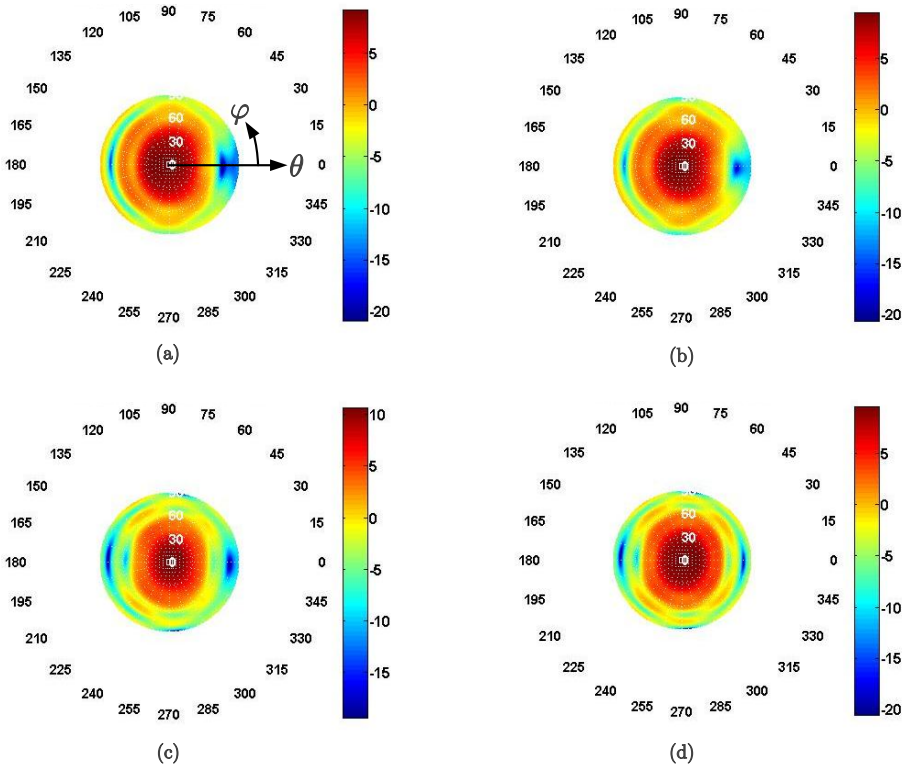

Figure 3.3: Radiation patterns as calculated by the CAESAR software. The different patterns correspond to different waveguide lengths. (a) 10.0 mm, (b) 12.5 mm, (c) 15.0 mm and (d) 17.5 mm.

3.2.2 Voltage Port Construction

Although the elements were first constructed and optimized using the FEKO software, it has been of crucial importance to cross-validate both the impedance matching and the radiation patterns with the CAESAR software. Accordingly, the antenna elements can then be used with confidence in the minimization algorithm. The element design proved quite difficult since the voltage port has been defined differently in the two programs: FEKO designates all mesh elements at the boundary between the voltage pin and the waveguide wall as part of the port, and excite the mode from the infinitesimal voltage gap boundary between these mesh elements. CAESAR, on the other hand, assigns the voltage port to be a single mesh cell, which must be specified as a separate polygon in the geometry definition. This complicated the cross-validation. In order to refine the mesh during the CAESAR simulations without "breaking up" the voltage port polygons into finer mesh elements, special "guard polygons" were constructed. The guard polygons are defined as low resolution triangles that keep their shape even if the surrounding mesh is refined. This makes it possible to retain a well-behaved voltage port occupying a single cell while refining the surrounding mesh. The overall mesh construction is still inherently different from the one in FEKO, however. A conceptual figure showing the different port constructions can be seen in Fig. 3.4.

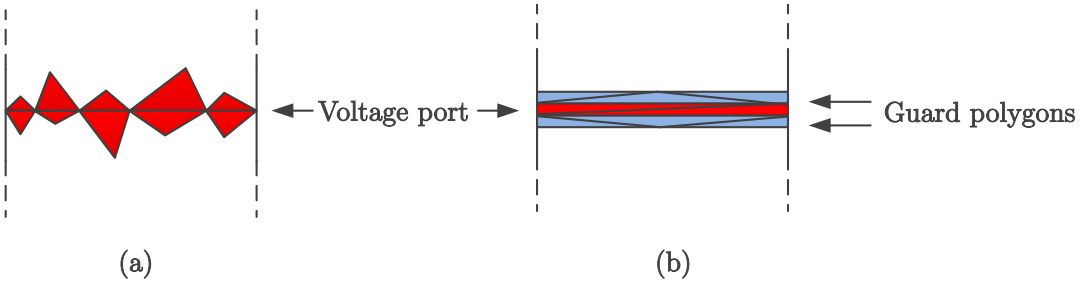

Figure 3.4: Conceptual sketch of the voltage port construction for different EM software programs. (a) A typical voltage port in FEKO. (b) A typical voltage port in CAESAR. Note especially the guard polygons in the CAESAR case.

3.3 Antenna Array Optimization

The antenna arrays have been optimized using the minimization algorithm described in Sec. 2.4. In the software it is possible to specify the size and shape of each desired array, the resolution of the element placement grid as well as the element type to be used. The radiation mask also needs to be provided and is a very important constraint from a system

point of view (as also mentioned in Sec. 1.2). The requirement of a narrow beam with low SLL directly affects the number of radiating elements and their placement onto the array grid. The choice of the threshold level for discriminating between active and passive elements is also of importance. Element weights that are less than the specified threshold level will be discarded from the final array configuration. Since all antenna array elements are included in the minimization process, the threshold should not be set too high to avoid that the solution will not be able to fulfill the specified radiation mask, and not too low so that redundant elements are included in the solution.

The given specifications in Table 1.1 states that scanning should be possible over the entire Earth's surface. There are several factors worth mentioning. Starting with Eq. (2.27), we see that scanning will degrade the directivity of the array; a scan angle of 8.69° would result in a degradation factor of $0.9885 = -0.0502\,\text{dB}$, a relatively small contribution. However, the element pattern gain has also degraded when observing a direction other than broadside, and because the array factor in (2.20) is multiplied by the element far-field function, the degradation of the total array pattern will be severely affected for large scan angles. Even though the scan angles are small, the effects must be taken into account in order to meet the specification requirements.

3.3.1 Scan Degradation

Since the element configuration is optimized for broadside illumination, the side lobes will start to increase when scanning. This problem is inherent to array antennas as scanning is accomplished by a linear phase shift. The phase shift produces a tilted wave front and the side that is advanced in phase relative to the center of the aperture will, for conventional phased array antennas, suffer from increased SLL. The same will happen to a sparse array if the optimization is only done for broadside illumination. The natural next step is then to present additional constraints on the solution in the form of one or more radiation masks so that scanning may be performed while suppressing unwanted side lobes.

Since the algorithm will take all constraints into account it consumes more time to find the solution. Hence, a good trade-off is needed which is done in the form of three constraints, i.e., one mask for broadside scan, one for the outer-most scan with $\varphi = 0$ and one mask for the outer-most scan angle illumination with φ set to the angle halfway in between the symmetry planes, see Fig. 3.5.

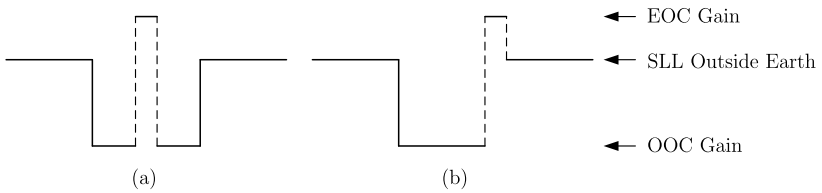

Figure 3.5: Conceptual examples of radiation mask constraints. (a) Mask for broadside illumination. (b) Mask for outer-most scan angle illumination.

3.3.2 Reduced Use of Synthesis Algorithm

Due to unforeseen events, the minimization algorithm that is being used throughout this thesis has limited functionality. The complete solution to the problem includes EM coupling effects, but these are not included in the solutions. The reason is that as the positions of the elements, as they are being adjusted during the second stage of the minimization process, get too close to each other. The algorithm fails as two or more array elements occupy the same space. The first step of the minimization process succeeds as this only utilizes isolated element patterns. See section 2.4 and figure 2.4 in particular for clarification. This means that the presented solutions is probably not the optimal ones since the last stage of the optimization is omitted. However, the second step of the optimization is mainly a refinement step. As the results from the first step of the algorithm in general gives good results, the gain of including EM coupling effects via the second optimization step is believed to be limited.

3.4 Demonstrator Construction Plan

The future demonstrator will be a "proof-of-concept" model and will be supplemented with economical cost constraints. The total cost for an array demonstrator has been approximated by RUAG Space to 5.000–10.000 SEK per array element and 20.000–30.000 SEK for other costs. Therefore, a complete set of elements (for an entire array antenna) with a complete distribution and beamforming network is not an option. Instead, the demonstrator will consist of a ground plane with pre-drilled holes for the elements, together with a small set of elements forming a sub-array that will be moved and measured in sequence. The embedded element pattern of the central element of this sub-array will then be saved and superimposed to the next embedded element pattern in order to acquire the total radiation pattern for the entire array. The final number of demonstrator elements that is feasible to manufacture is decided by RUAG Space. The present number lies somewhere

between 10 and 15. The preferred approach is to solve a local environment using the Characteristic Basis Function Method (CBFM), a method that has been incorporated in the CAESAR software, and to compare this local environment to that of the reference solution incorporating all array elements.

The number of elements that will be needed is calculated as follows. First, an initial solution by employing only isolated elements is obtained. From this solution, an element is chosen whose number of neighboring elements in a locally defined environment is large, after which its embedded element pattern for the complete array layout is calculated. Upon denoting this pattern as the reference pattern, we then calculate the pattern of that same element, but in isolation, and call this the local pattern. Next, we find the errors δ_{CO} and δ_{XP} as

$$\delta_{\mathrm{CO}} = \frac{1}{|\mathbf{G}_{\mathrm{CO,ref}}(0)|N} \sum_{\theta=-N/2}^{N/2} |\mathbf{G}_{\mathrm{CO,loc}}(\theta) - \mathbf{G}_{\mathrm{CO,ref}}(\theta)| \tag{3.2}$$

$$\delta_{\mathrm{XP}} = \frac{1}{|\mathbf{G}_{\mathrm{CO,ref}}(0)|N} \sum_{\theta=-N/2}^{N/2} |\mathbf{G}_{\mathrm{XP,loc}}(\theta) - \mathbf{G}_{\mathrm{XP,ref}}(\theta)| \tag{3.3}$$

These errors correspond to the error in the co- and cross-polar far-fields, respectively. They consist of the arithmetic mean of the error taken over all calculated θ angles, and are then normalized to the co-polar broadside gain. The co- and cross-polar errors are of equal importance in order to reach convergence, since the system is intended for circular polarization.

After the errors have been calculated, we define a small circle centered over the active element and increment its radius until at least one more element is included. We then proceed to calculating the embedded element pattern when only these two or more elements are present and update the local pattern with this newly obtained pattern.[1] After this, we calculate new co- and cross-polar errors in the same manner as previously and iterate until the errors drop below some specified threshold. At this point, important data such as number of included elements and radiation patterns are saved. Fig. 3.6 summarizes the procedure. There is no rule as to what relative error level should be reached before calling it convergence, but a reasonable figure is 1 %, which converts to -40 dB. This is the active element threshold that is chosen in the array synthesis process. It is also in the regime of the XPD level for the array elements.

[1]The acquired pattern is called the local pattern since it is calculated from a local set of array elements, defined by small circle centered around the element of interest.

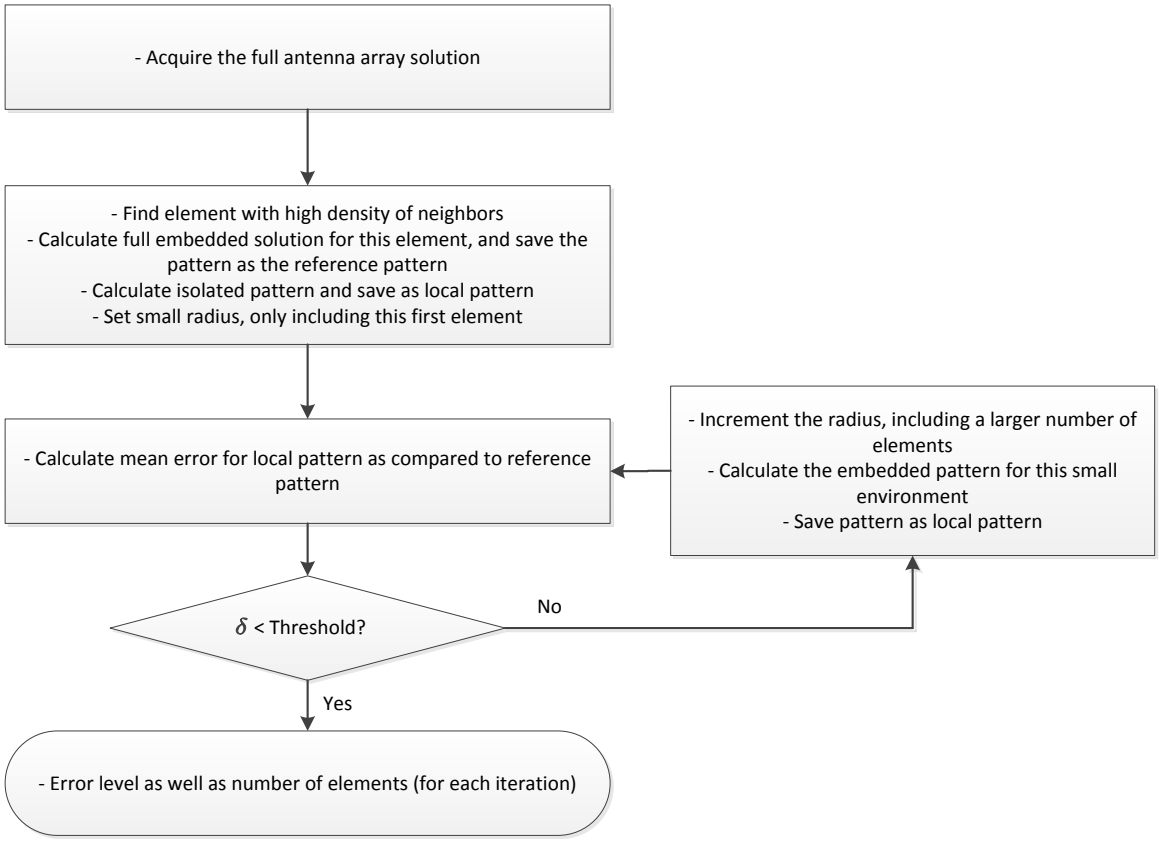

Figure 3.6: Algorithm to decide on the minimum number of elements that is needed for constructing the physical demonstrator.

Chapter 4

Numerical Results

This chapter constitutes the numerical results section, which is subdivided into three parts: the array element simulations and their construction, the full array designs synthesized through the optimization algorithm, and a discussion of the results in the light of different computational aspects as well as the approach to constructing a demonstrator. The element design has resulted in three main candidates: The corrugated pipe horn designed at RUAG Space, and two versions of a pyramidal horn, utilizing different aperture sizes in order to examine the effect of different element gains on the array synthesis. A summary of the array elements is provided. The full array synthesis is presented next. Two separate array aperture sizes, corresponding to two different spot sizes, were considered for each of the three array element types. The chapter also provides recommendations as for which candidates are suitable for construction, and the convergence behavior for these candidates. The last section discusses the previously acquired results.

4.1 Element Simulations

As discussed in Sec. 3.2, a few different element types were simulated in order to consider a variety of different gain and EM coupling characteristics in the antenna array synthesis process. This part of the work is important in order to evaluate the impact of different elements on the final array solution, but also served the purpose of learning the CAESAR software. The corrugated pipe horn is an array element that has been designed and suggested as one of the candidate antennas by RUAG Space. In addition, a large, as well as a small, pyramidal horn are evaluated. The geometry of these horns are almost identical, except for the flare length, which differs by a factor of two. The reason for picking two versions of the same horn is that it is desired to investigate what impact the element gain

has on the final synthesized array layout.

As mentioned in Sec. 3.2, the voltage ports are defined differently in the CAESAR and FEKO software. Using the pyramidal horn cross section, we illustrate the initial setup in Fig. 4.1. Note that the monopole illustration shows the CAESAR geometry. Here, the distance between the end of the monopole and the waveguide wall was kept constant with the voltage port placed in-between. Fig. 4.2 shows the reflection coefficient for the case when the monopole is elongated, while maintaining the distance between the end of the monopole and the voltage port between the solvers. Finally, in Fig. 4.3 the total pin length includes 2/3 of the total voltage port extension. In addition, the voltage port polygon and the surrounding guard polygons (see Fig. 3.4) was thinned by a factor 3.5, i.e., from $\lambda/100$ to $\lambda/350$. The change in voltage pin length is thus no more than $\lambda/30$, which is about the size of one mesh element in the simulations, while the impact on the reflection coefficient spans several orders of magnitude. Since the case in Fig. 4.3 resembles the FEKO port the most from a geometrical point of view, it is indeed expected that this is the case where the reflection coefficient resembles the FEKO simulation the most.

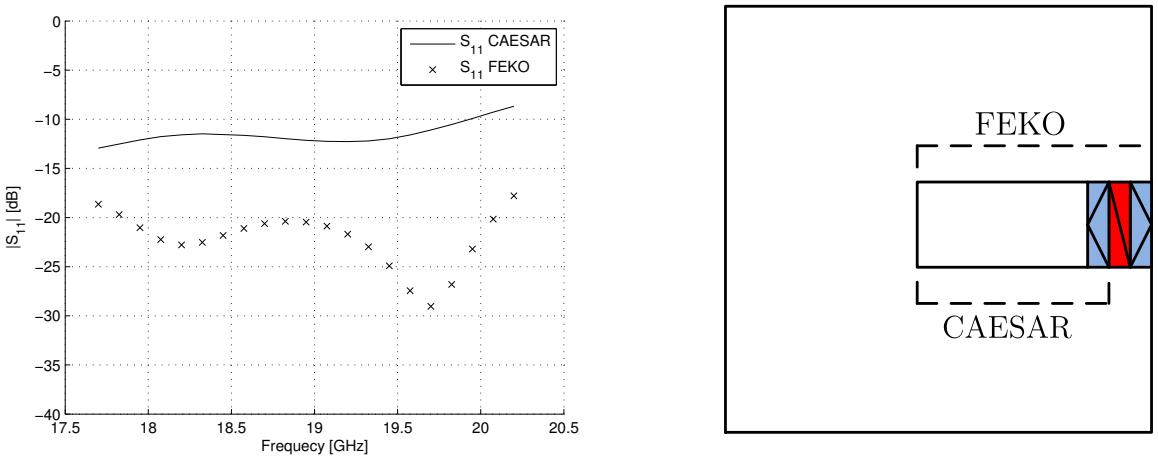

Figure 4.1: $|S_{11}|$ for the large pyramidal horn. This figure compares CAESAR and FEKO as the distance between the voltage pin end and the waveguide wall is the same between the two solvers. Note that the voltage port is defined as in the CAESAR software.

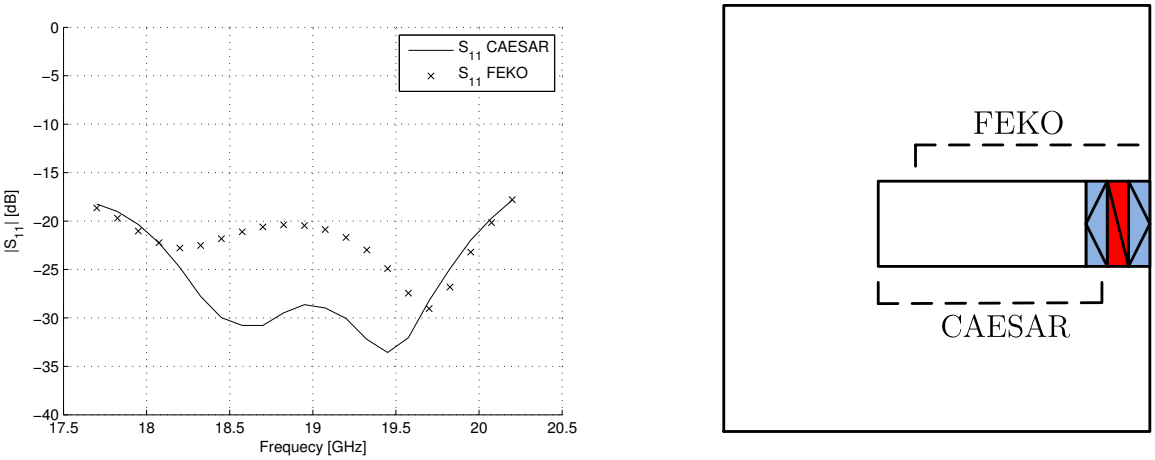

Figure 4.2: $|S_{11}|$ for the large pyramidal horn. This figure compares CAESAR and FEKO as the distance between the end of the monopole and the voltage port is the same between the two solvers.

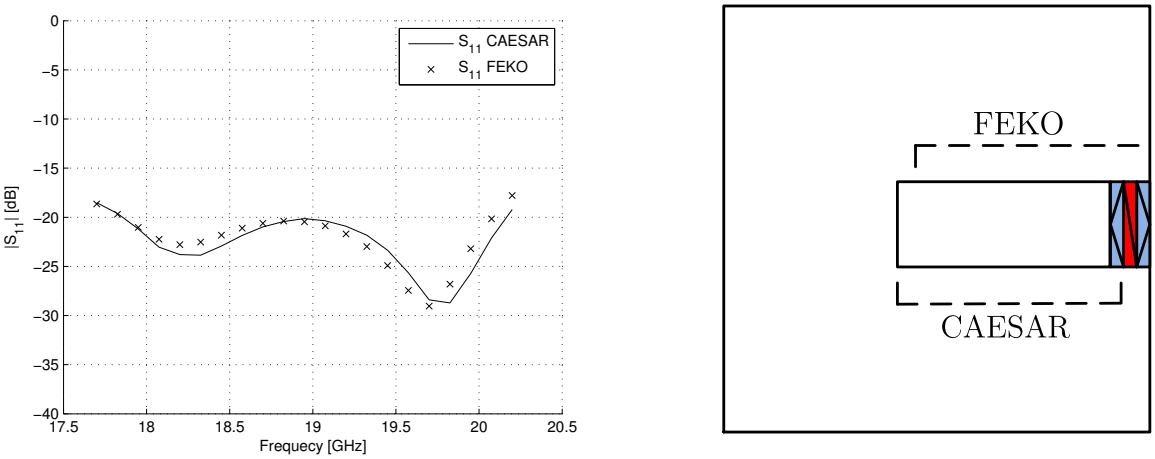

Figure 4.3: $|S_{11}|$ for the large pyramidal horn. This figure compares CAESAR and FEKO as the CAESAR voltage port is thinned and the monopole includes 2/3 of the voltage port extension.

4.1.1 Corrugated Pipe Horn

The corrugated pipe horn was designed at RUAG, and the geometry as constructed in CAESAR is illustrated in Fig. 4.4. Due to differences in how the elements are constructed in the different types of software, the impedance matching appear different; while meshing in FEKO is performed from a geometrical definition, the corrugated pipe horn made in CAESAR is meshed from individual polygons. Even though the resolution is limited in both CAESAR and FEKO, the approach to constructing geometries are inherently different in the two programs, yielding different full-wave solutions. Fig. 4.5 illustrates the difference.

The overall gain is about 8 dBi and the aperture size is about 510 mm^2. The matching over the TX band and the gain for the center frequency has been plotted in Fig. 4.6. The figure shows a rather flat gain profile, even outside Earth coverage, and, for the FEKO case, a reasonably low reflection coefficient over the whole TX band. It also shows the large difference in calculated impedance matching over the TX band.

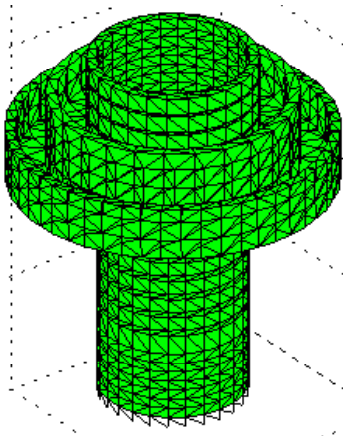

Figure 4.4: Geometry of the corrugated pipe horn, as constructed in the CAESAR software.

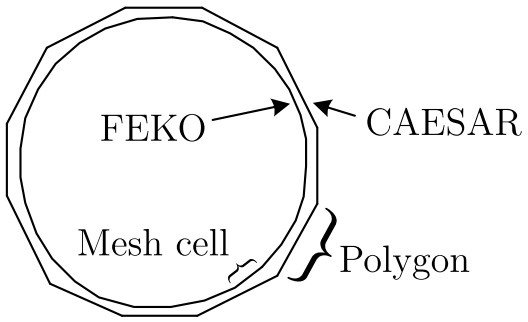

Figure 4.5: The method of constructing geometries is inherently different in the CAESAR and FEKO software.

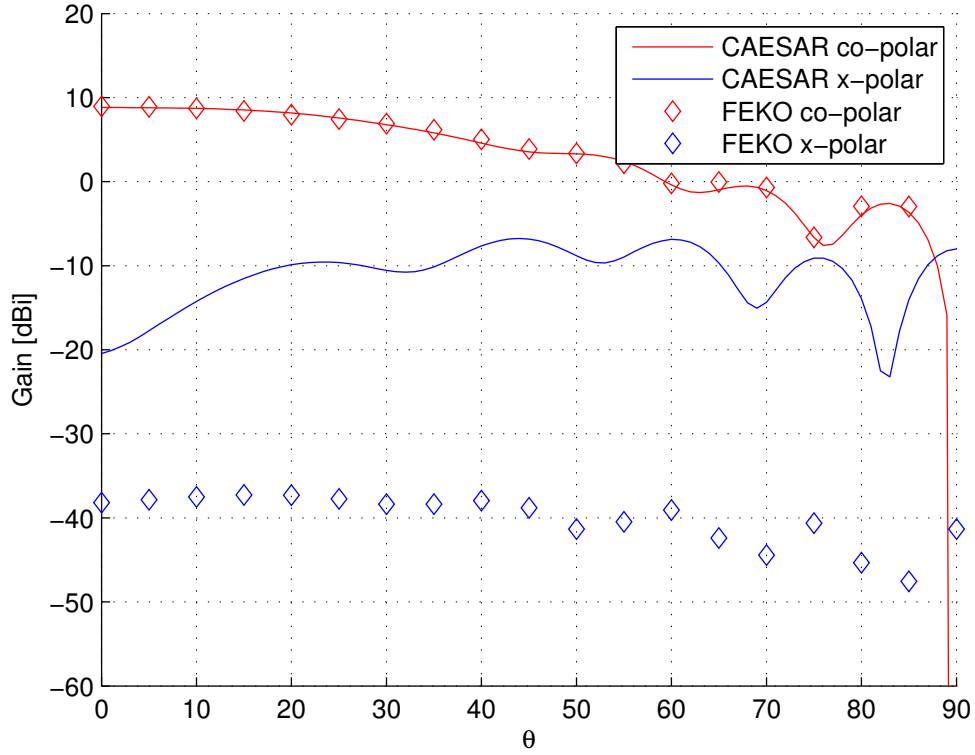

(a)

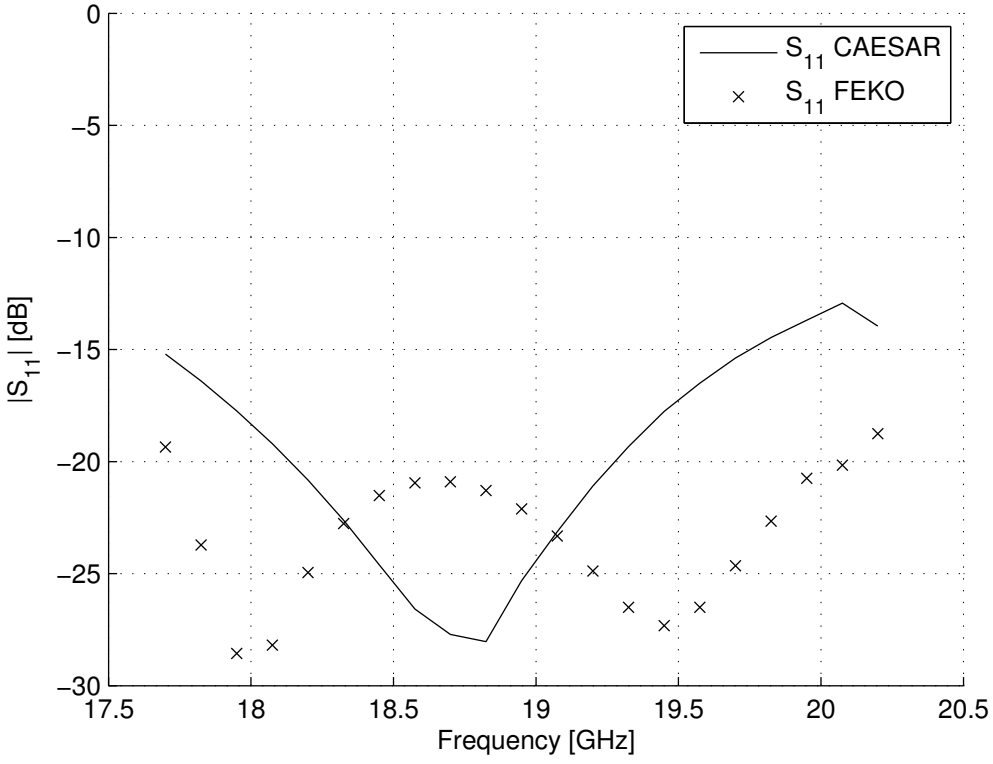

(b)

Figure 4.6: Characteristics of the corrugated pipe horn, calculated in both CAESAR and FEKO. (a) Gain. (b) $|S_{11}|$.

4.1.2 Small Pyramidal Horn

The concept of using pyramidal horns is quite appealing as its construction is well-known and can be excited to radiate both right- and left handed circular polarization. The simple geometry allows for a robust, all-metal array element with low construction cost. Horn arrays have been used both as radiating array elements as well as reflector antenna feeds. The primary factor to take into account regarding the element geometry is to miniaturize the element as much as possible. This enables a large placement flexibility, as discussed in Sec. 3.2. The waveguide section is chosen large enough to allow only the fundamental mode of the lowest specified frequency in the TX band to propagate up to the horn section. The flare angle was optimized using the FEKO software, and the gain of the antenna was changed by changing the flare length. As shown in Fig. 4.8, the gain at broadside is 10.8 dBi and the impedance matching lies below -19 dB over almost the entire TX band.

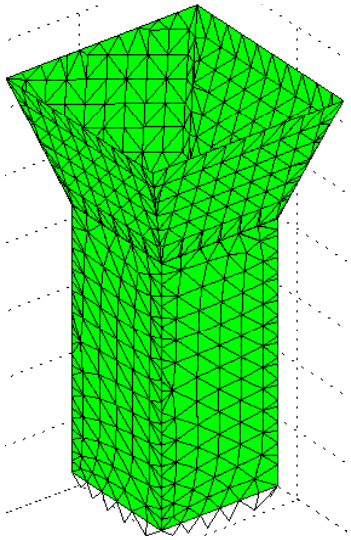

Figure 4.7: Meshed geometry for the small pyramidal horn as constructed in the CAESAR software.

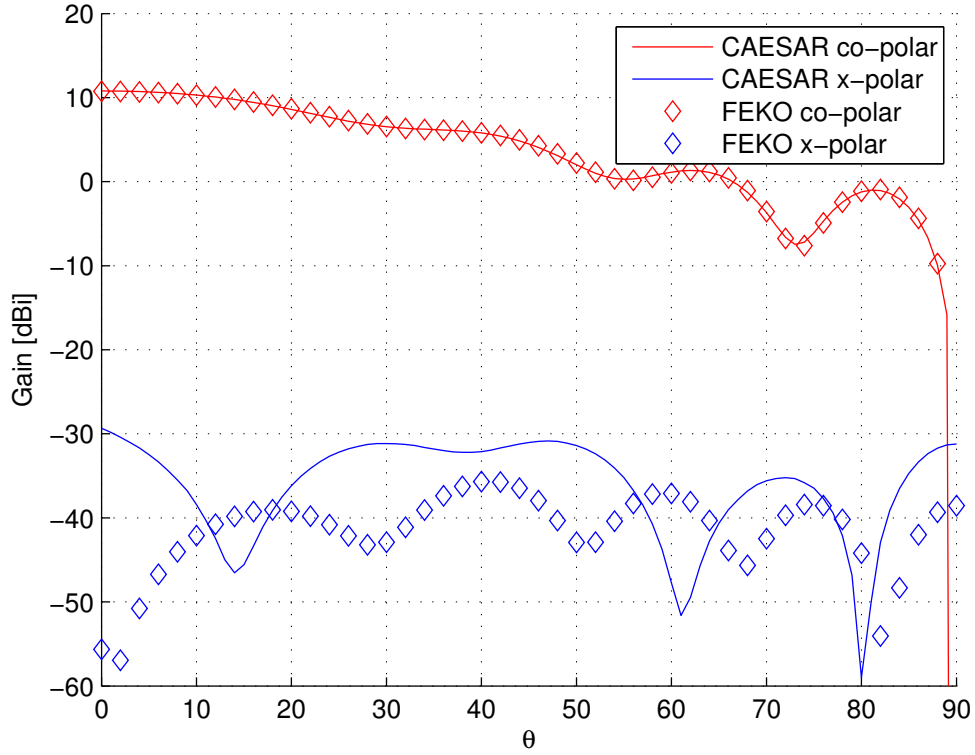

(a)

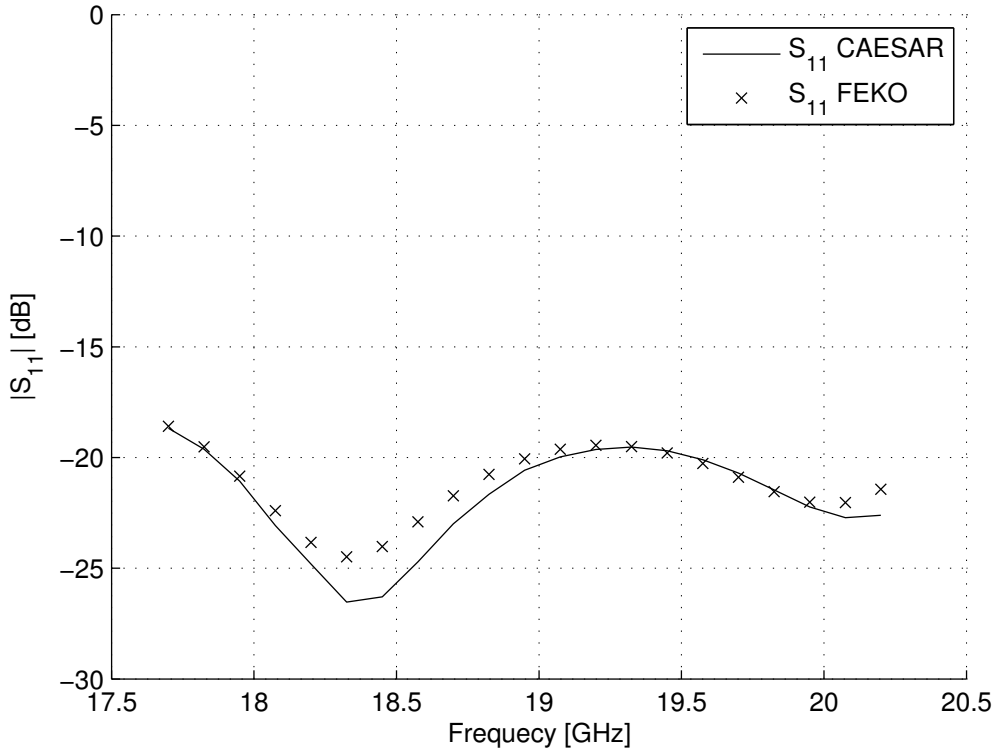

(b)

Figure 4.8: Impedance and radiation characteristics of the small pyramidal horn as calculated by the CAESAR and FEKO software. Comparison of: (a) Calculated gain, and; (b) The reflection coefficient.

4.1.3 Large Pyramidal Horn

The geometry of the large pyramidal horn is shown in Fig. 4.9. It has a longer flare which results in a gain of 13.6 dBi at broadside as can be seen in Fig. 4.10, where both the gain and the reflection coefficient of the large pyramidal horn case are illustrated. Note that the gain is higher and tapers off faster, which is to be expected.

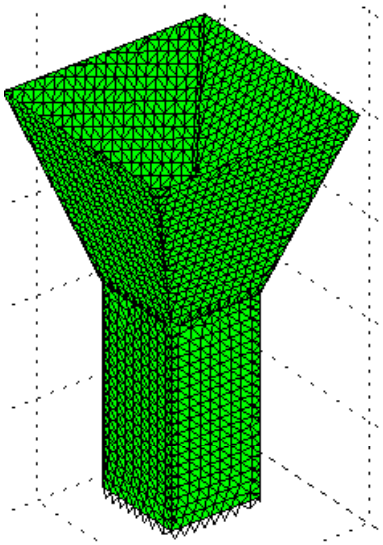

Figure 4.9: Meshed geometry for the large pyramidal horn as constructed in CAESAR.

A comparison between the gain of a set of pyramidal horns with different flare lengths is illustrated in Fig. 4.11(a). From this figure, one observes that the gain rises as the flare length and the aperture area increases. Due to the phase error introduced by the spherical wave front at the aperture, however, the gain does not increase as fast as the aperture area, rendering the largest horn rather uneconomical from a flexibility point of view. From this observation the decision was made to include only two of the three simulated pyramidal horns, i.e., the two smallest ones. Thus, the horns that are mentioned as the small and large pyramidal horns above, are those corresponding to the short and the medium flare lengths in Fig. 4.11(a). Furthermore, Fig. 4.11(b) shows that the flare length has an impact on the impedance matching as well. The difference in impedance matching persists despite the approach of separating the parts during its optimization as described in Sec. 3.2.1. This subfigure also aided in the decision making to exclude the largest horn from the array synthesis process. Even though it is better matched in the center of the band, it is well above -20 dB for most of the band, which is unacceptable.

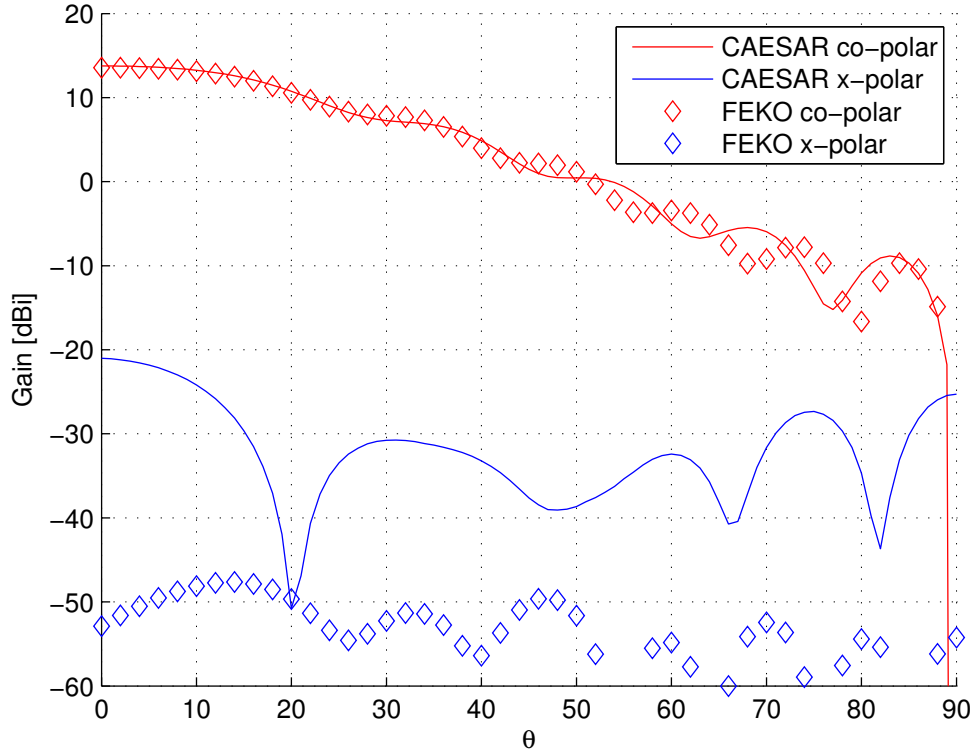

(a)

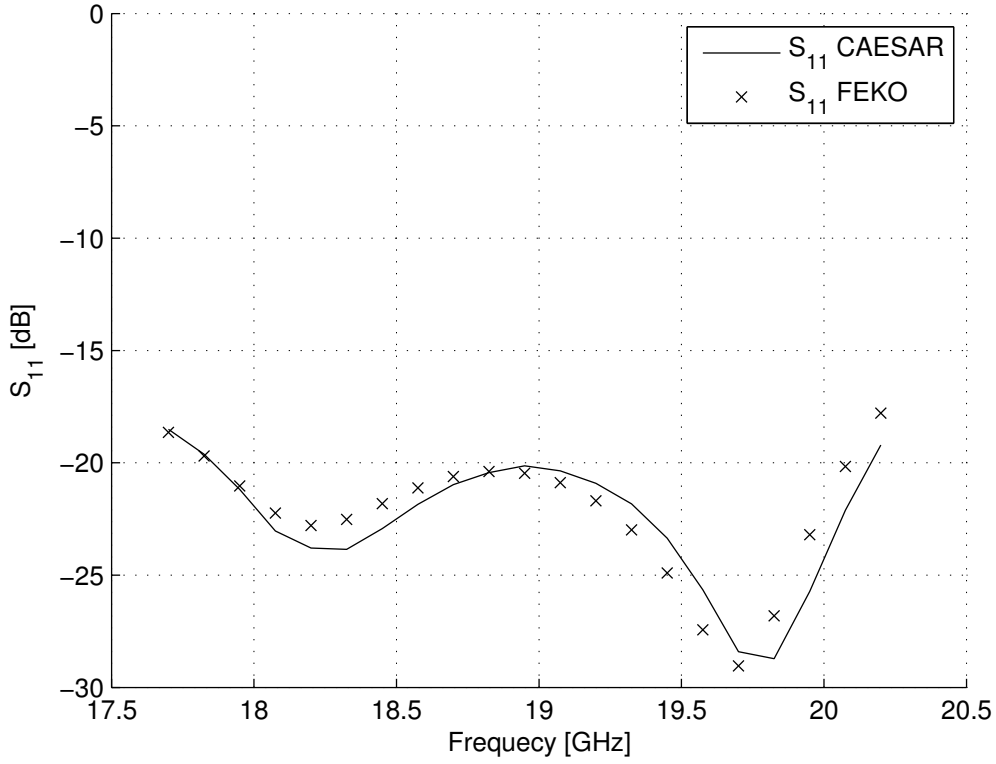

(b)

Figure 4.10: Impedance and radiation characteristics of the large pyramidal horn as calculated by the CAESAR and FEKO software. Comparison of: (a) Calculated gain, and; (b) The reflection coefficient.

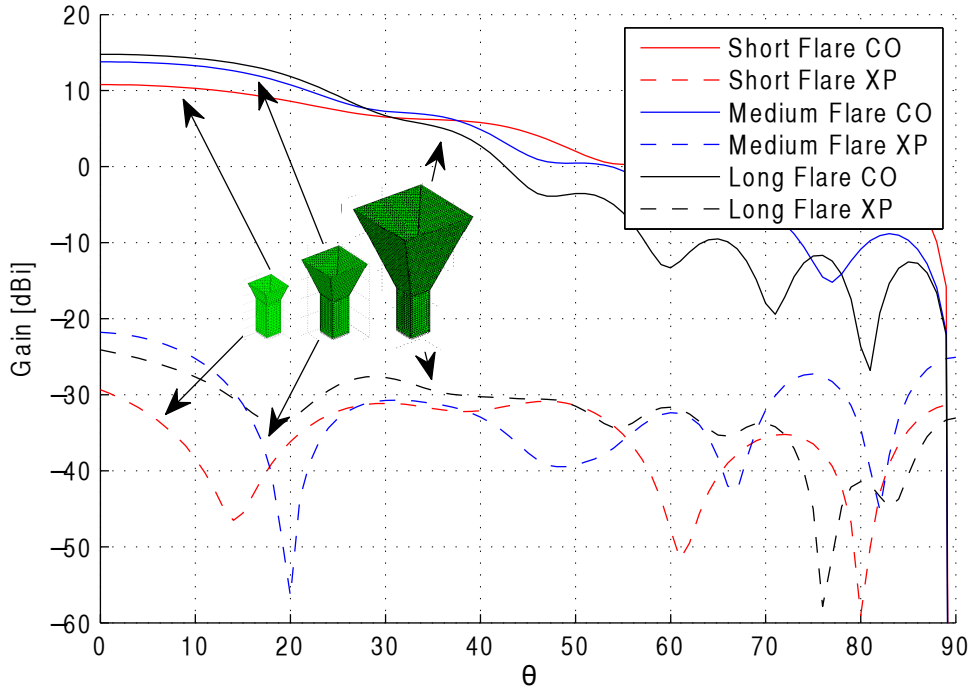

(a)

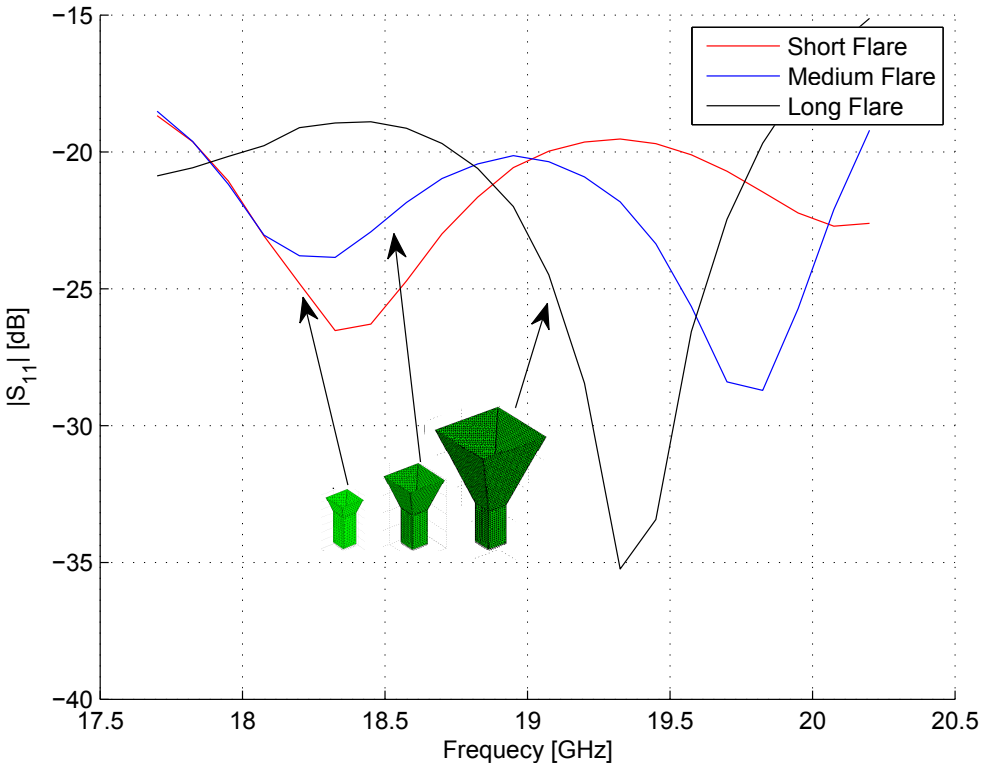

(b)

Figure 4.11: Implications of different flare lengths on the pyramidal horn. (a) Gain for different flare lengths. (b) $|S_{11}|$ for different flare lengths.

4.1.4 Summary on the Element Simulations

The elements that are simulated will be employed as antenna array elements and are designed to meet the initial specifications in Table 1.1. All element types presented in this section provide sufficiently high gain inside the AOC, as well as sufficiently good impedance matching inside the whole TX band. They also provide sufficiently high Cross-Polar Discrimination (XPD) inside the AOC. Since the XPD differs significantly between the different solvers, the tabulated value refers to the worst-case XPD, provided by the CAESAR software. The reason for the large difference in XPD between CAESAR and FEKO could be the fact that CAESAR is not designed for accurate results below -30 dB. This is a feature of CAESAR, implemented in order to maintain high computational performance. The results are summarized in Table 4.1, where Return Loss (RL) denotes the negative reflection coefficient in dB. Details about the pyramidal horn geometries are provided in Appendix A.

Table 4.1: Summary for the considered array elements, sorted by increasing gain. For the XPD, the mentioned interval describes the worst-case value inside the Earth's coverage. For the RL, the interval describes the worst-case difference inside the TX band.

Element type	Broadside Gain [dBi]	XPD [dB]	RL [dB]	Area [mm^2]
Corrugated Pipe Horn	8.1	24.1–28.8	19.5–31.2	510
Small Pyramidal Horn	10.8	39.8–46.5	18.5–26.5	238
Large Pyramidal Horn	13.6	33.6–35.8	18.5–28.7	459

4.2 Array Simulations

This section presents the array simulations utilizing the different element candidates. All candidates employ a so called eight-fold symmetry, meaning that the array elements in a circular array are placed in eight identical slices rotated around a central point. Thus, the array will repeat itself after being rotated 45°. Each subsection contains one candidate realizing the minimum specified spot size of 0.5° and one candidate realizing a maximum specified spot size of 1° according to Table 1.1. In the following section these will be referred to as the small and large spot size, respectively.

The results for the array simulations are organized by element type. The results for each element type is presented by means of (i) The array configuration: In the following plots, the location and size of the array elements are shown with one of the symmetry slices marked out. The dots at each element placement represent the central coordinate of each element, while the circle around it indicates the outer rim of the aperture. This plot

clearly reveals any collisions occurring between elements, which will prevent a physical array antenna from being constructed. (ii) Scanning: The scanning performance is shown in the $\varphi = 0°$ plane. Scanning the array is performed by means of an ideal linear phase shift (see section 2.2.1). (iii) Scanning is also shown for the $\varphi = 0°$, $\varphi = 45°$ and $\varphi = 90°$ planes, illustrating the entire pattern with the aid of a mesh plot.

4.2.1 Arrays Using Corrugated Pipe Horns

For the corrugated pipe horn array simulations we start by looking at the array configuration satisfying the small spot size constraint. The array configuration utilizes 481 elements, and is shown in Fig. 4.12. For this particular array candidate element collision can be spotted close to the center as well as at the outer rim of the array. Fig. 4.13 shows the array being scanned in the $\varphi = 0$ plane. Here, it can be seen that the scanned beam follows the SLL mask quite well. The complete radiation pattern as scanning is initiated is shown in Fig. 4.14.

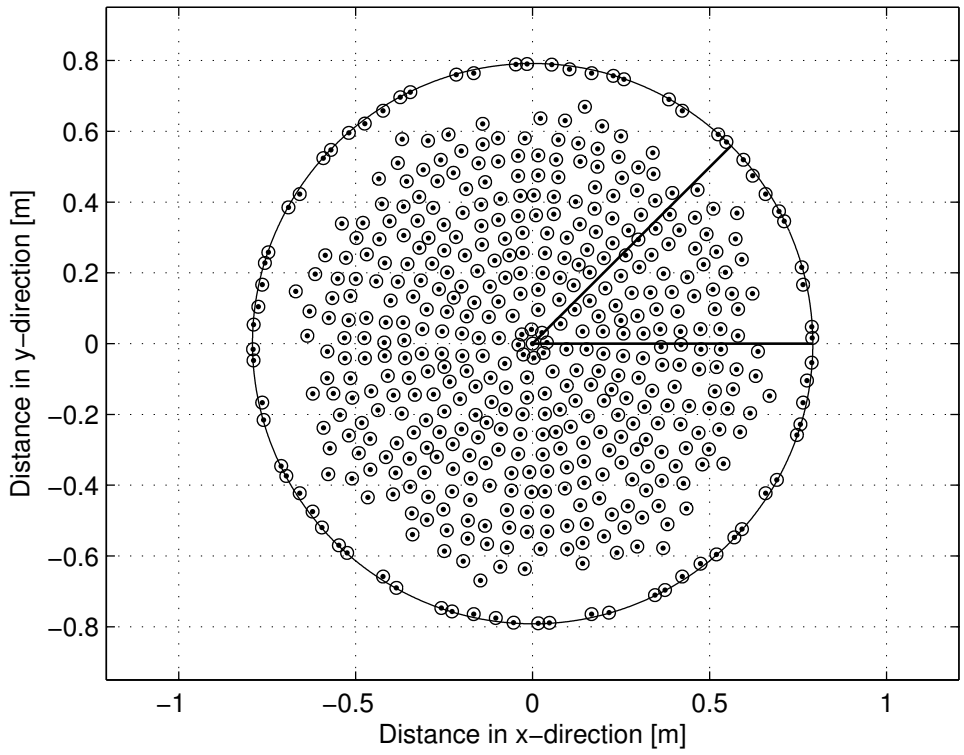

Figure 4.12: The synthesized configuration for the small spot size of 0.5°, utilizing the corrugated pipe horn.

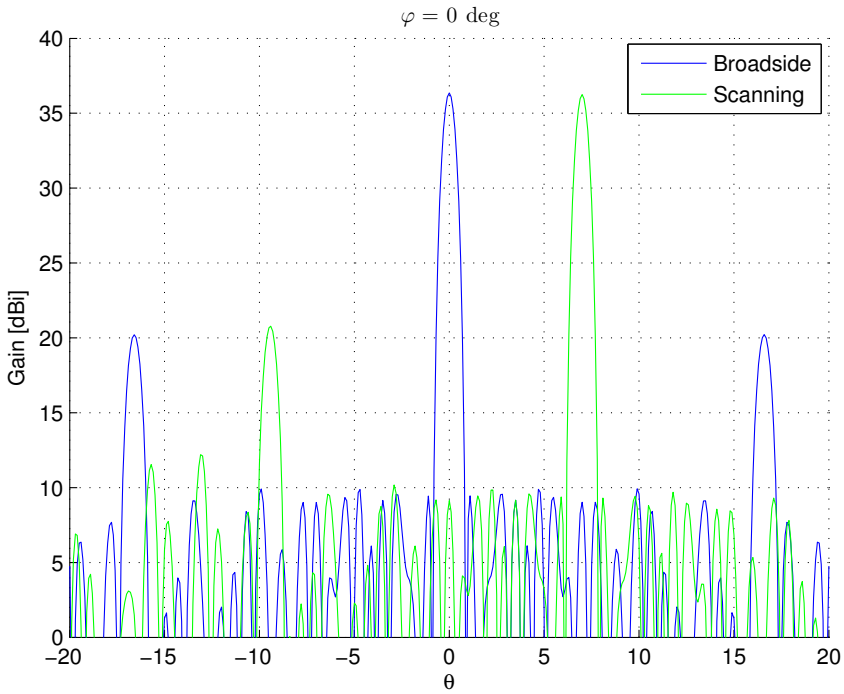

Figure 4.13: Scan behavior in the $\varphi = 0°$ plane using the corrugated pipe horn for acquiring the small spot size.

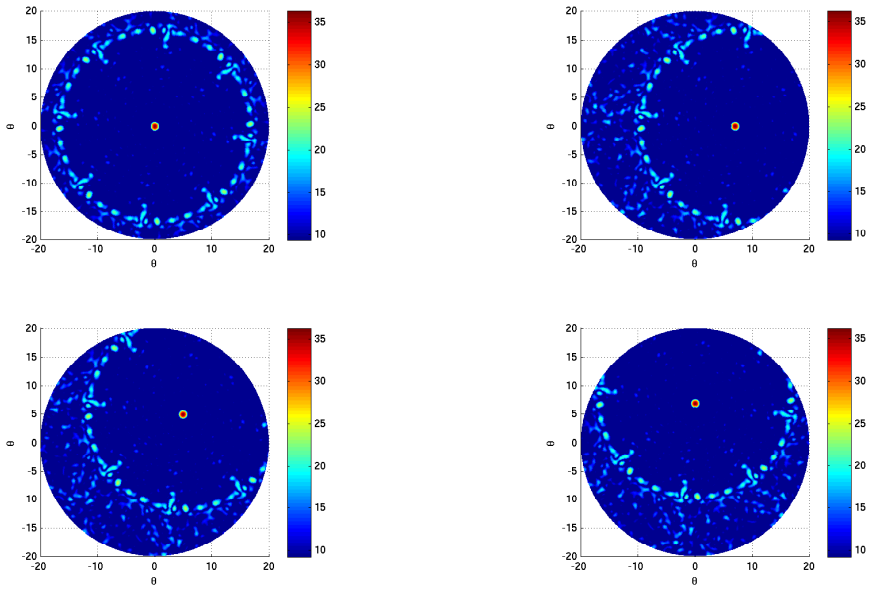

Figure 4.14: Radiation pattern as scanning is initiated using the corrugated pipe horn for the small spot size.

The results for the larger spot size are presented in a similar fashion. The plot of the overall configuration is shown in Fig. 4.15, using 193 elements. The scanning of this array is performed in the same way as described above, and the results are shown in Fig. 4.16. The overall behavior of the array is shown in Fig. 4.17, where the complete radiation pattern is shown when being scanned in several φ planes.

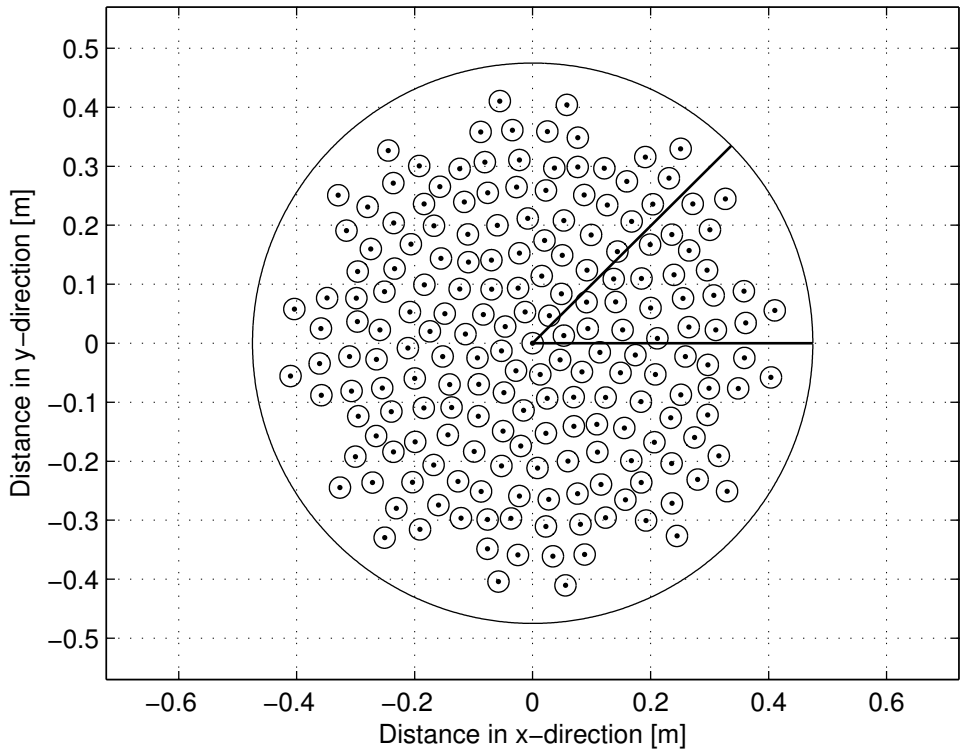

Figure 4.15: Here, the corrugated pipe horn is utilized in order to synthesize a configuration for the large spot size of 1°.

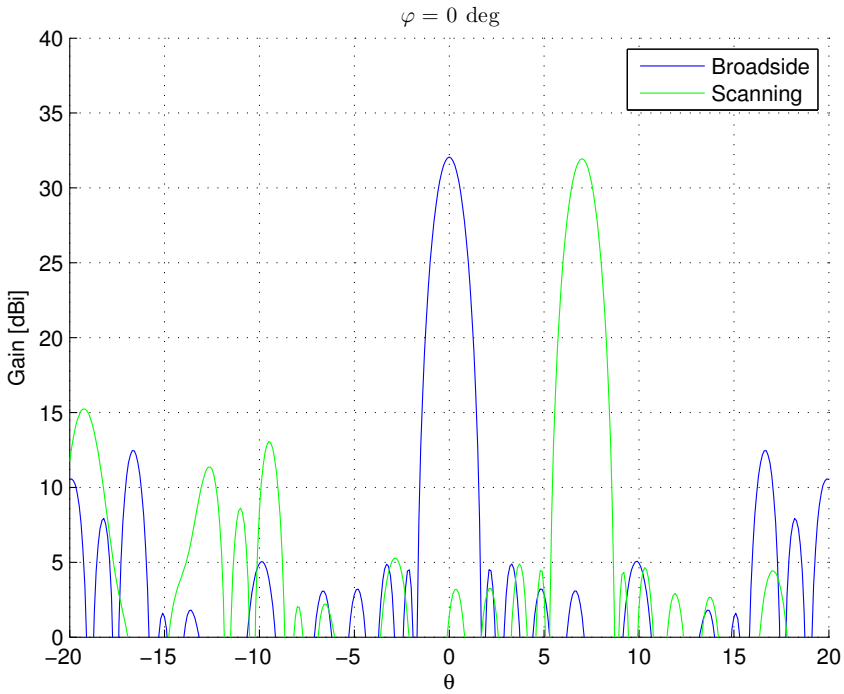

Figure 4.16: Using the corrugated pipe horn for the large spot size in order to scan the array in the $\varphi = 0°$ plane.

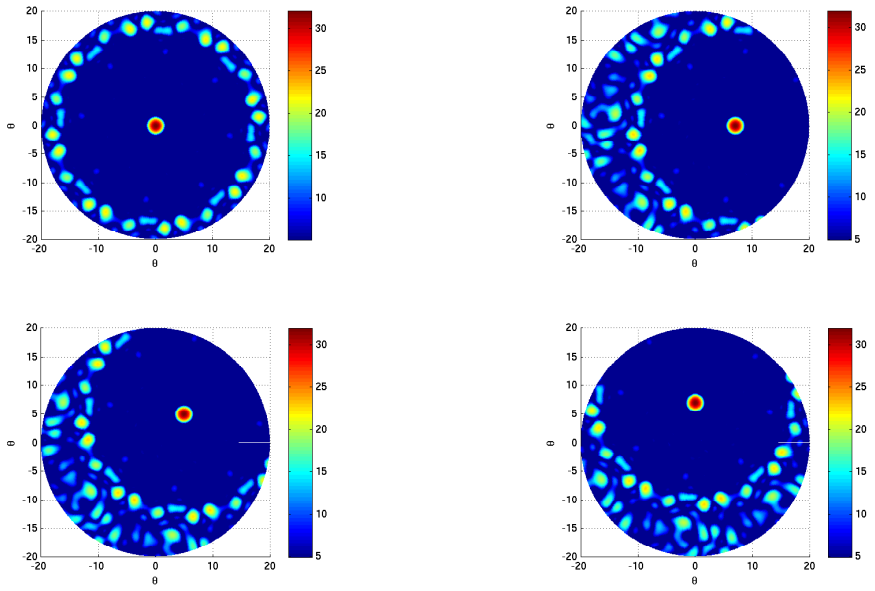

Figure 4.17: Scanning the array in several φ planes using the corrugated pipe horn, acquiring the large spot size.

4.2.2 Arrays Using Small Pyramidal Horns

As in the previous subsection, we start by presenting the array configuration yielding the small spot size. This candidate consists of 481 elements, and Fig. 4.18 shows the resulting element configuration. Note that the circles representing the aperture are smaller than the previous and upcoming cases, which allows for a larger placement flexibility. Since these elements have a square element aperture, this definition of the element boundary is somewhat conservative. Scanning using ideal linear phase shift is tested for the $\varphi = 0°$ in Fig. 4.19. Scanning in the same φ plane, as well as the $\varphi = 45°$ and $\varphi = 90°$ planes, is shown in Fig. 4.20.

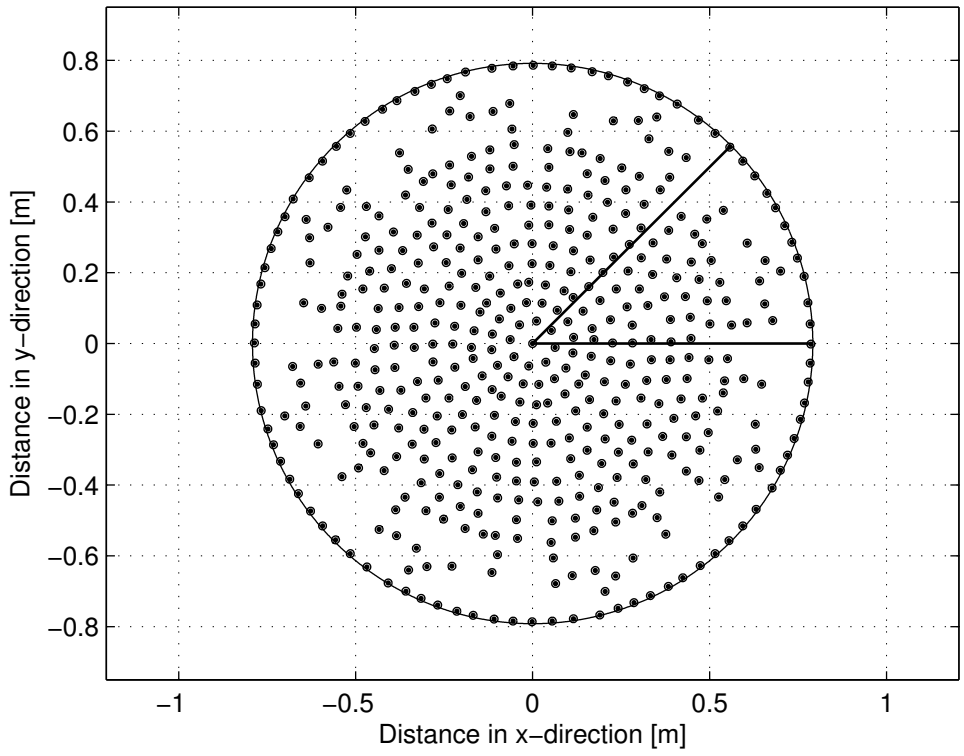

Figure 4.18: The synthesized configuration for the small spot size of 0.5°, utilizing the small pyramidal horn.

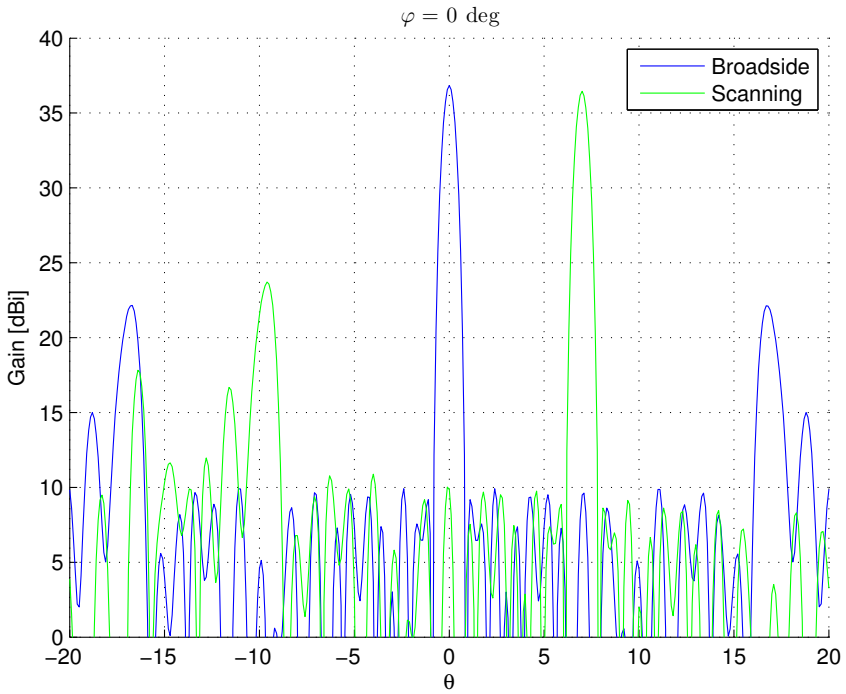

Figure 4.19: Using the small pyramidal horn for the small spot size while scanning in the $\varphi = 0°$ plane.

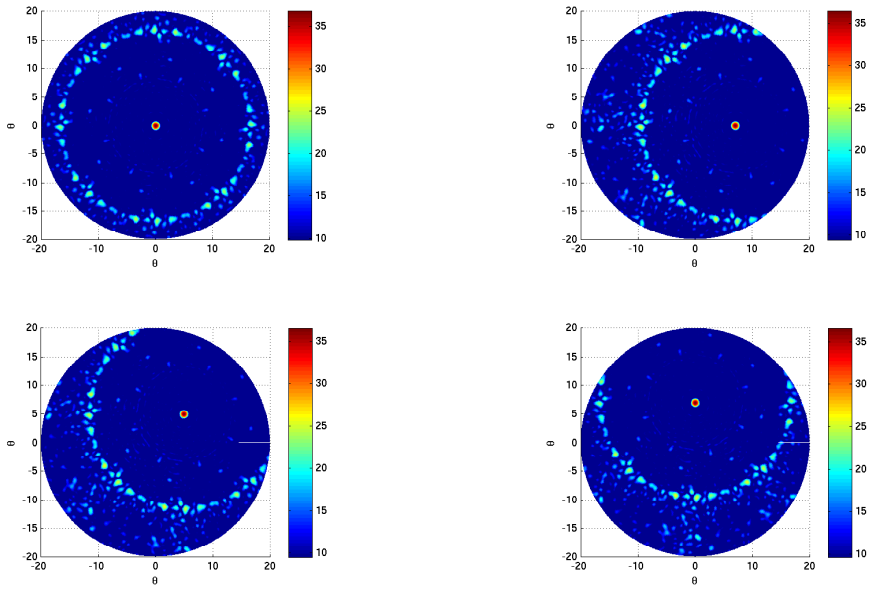

Figure 4.20: The complete radiation pattern is shown while the array with the small pyramidal horn and the small spot size is being scanned.

The upcoming array candidate utilizes 209 elements in order to synthesize an array for the large spot size. This yields the configuration shown in Fig. 4.21. In addition, Fig. 4.22 shows the scanning performed for the $\varphi = 0°$ plane, and finally, Fig. 4.23 shows the overall behavior of the array when scanned.

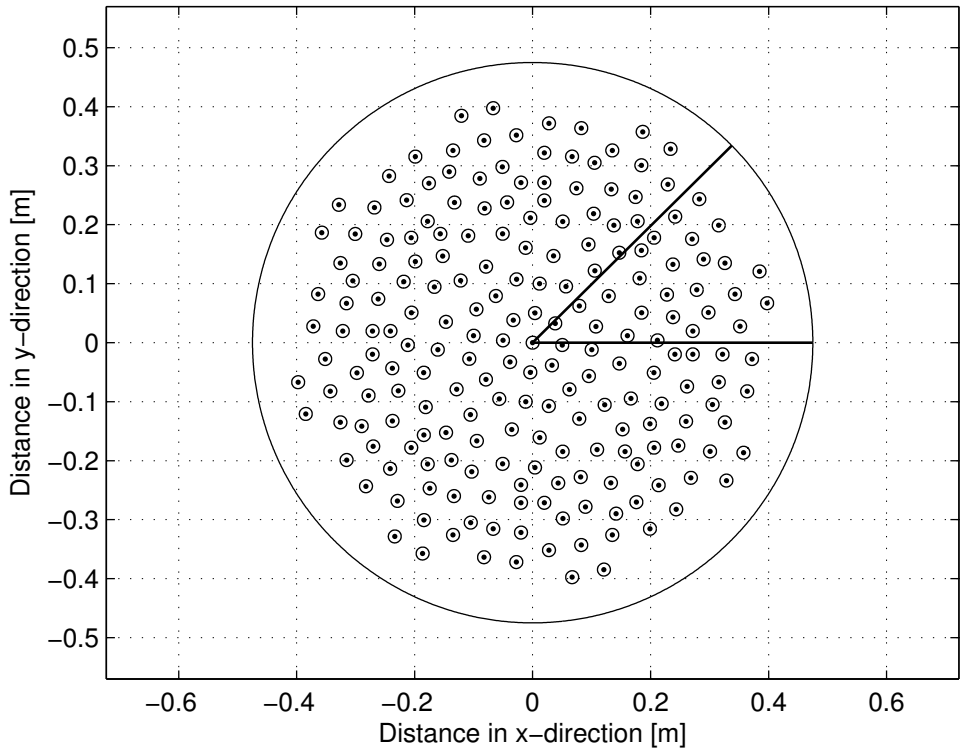

Figure 4.21: The synthesized configuration for the large spot size of 1°, utilizing the small pyramidal horn.

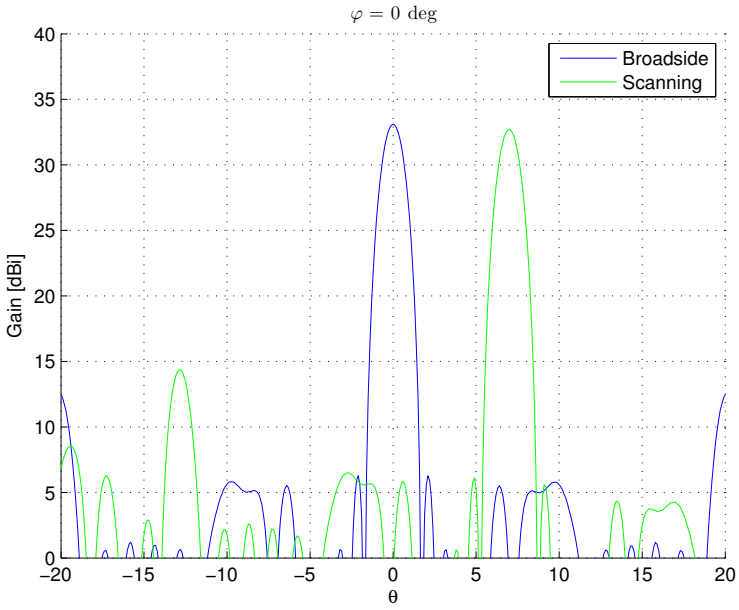

Figure 4.22: Scanning is shown for the large spot case utilizing the small pyramidal horn. Scanning is performed in the $\varphi = 0°$ plane.

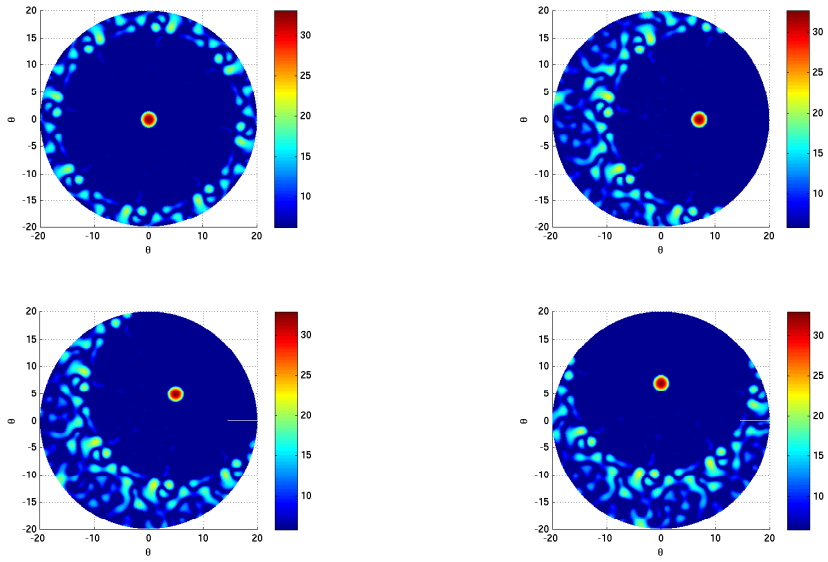

Figure 4.23: In the case of the small pyramidal horn and the large spot size, the complete radiation pattern is shown during scanning.

4.2.3 Arrays Using Large Pyramidal Horns

Fig. 4.24 shows the resulting element configuration for the large pyramidal horn, corresponding to the smaller spot size. As in the case of the small pyramidal horn, these elements have square element apertures, rendering the definition of the element boundary somewhat conservative. This array configuration use 441 elements in order to create the requested spot size. Furthermore, scanning is illustrated for the $\varphi = 0°$ plane in Fig. 4.25. More scan angles are illustrated in Fig. 4.26, where the entire radiation pattern is shown.

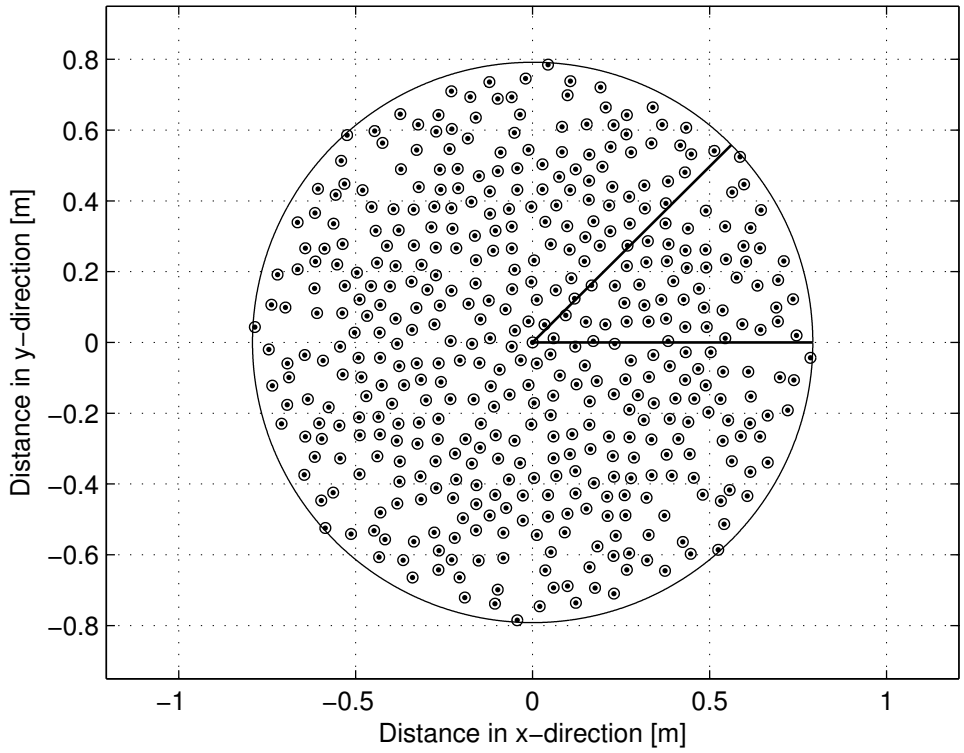

Figure 4.24: The synthesized configuration for the small spot size of 0.5°, utilizing the large pyramidal horn.

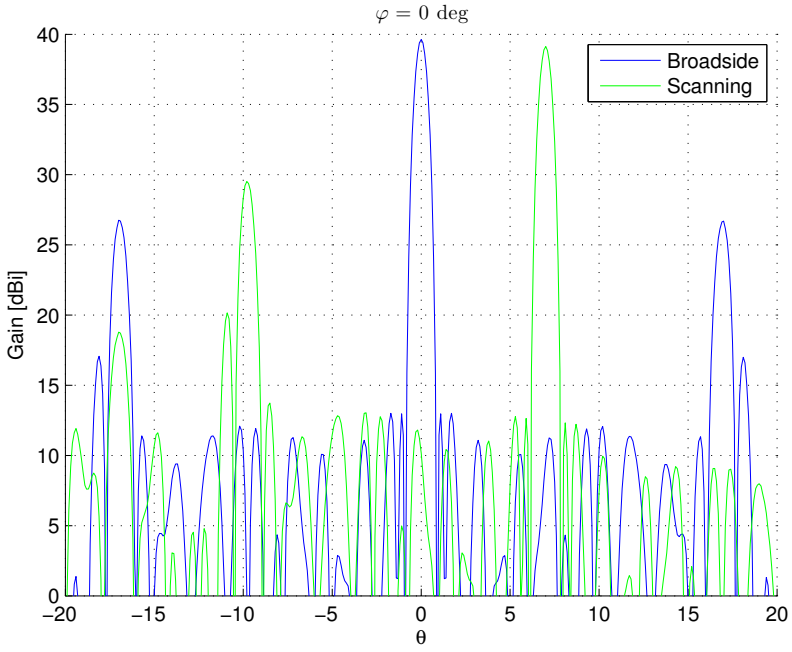

Figure 4.25: Scanning is shown for the $\varphi = 0°$ plane, using the large pyramidal horn for the small spot size.

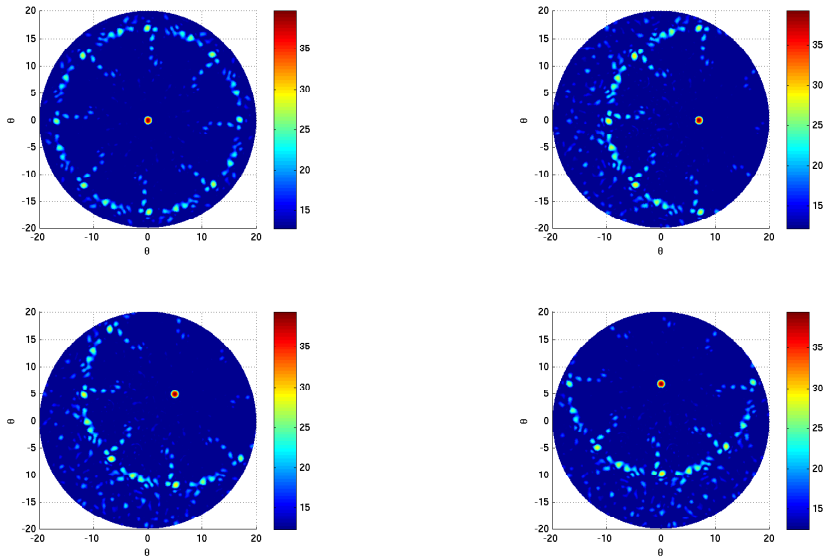

Figure 4.26: The complete radiation pattern is shown while the array with the large pyramidal horn and the small spot size is being scanned.

The total configuration yielding the large spot size is shown in Fig. 4.27. In addition, Fig. 4.28 shows the scanning performed in the $\varphi = 0$ plane, and finally, Fig. 4.29 shows the overall radiation pattern of the array when being scanned in several φ planes. This candidate need to include 177 elements in the array configuration, the lowest number of all presented candidates.

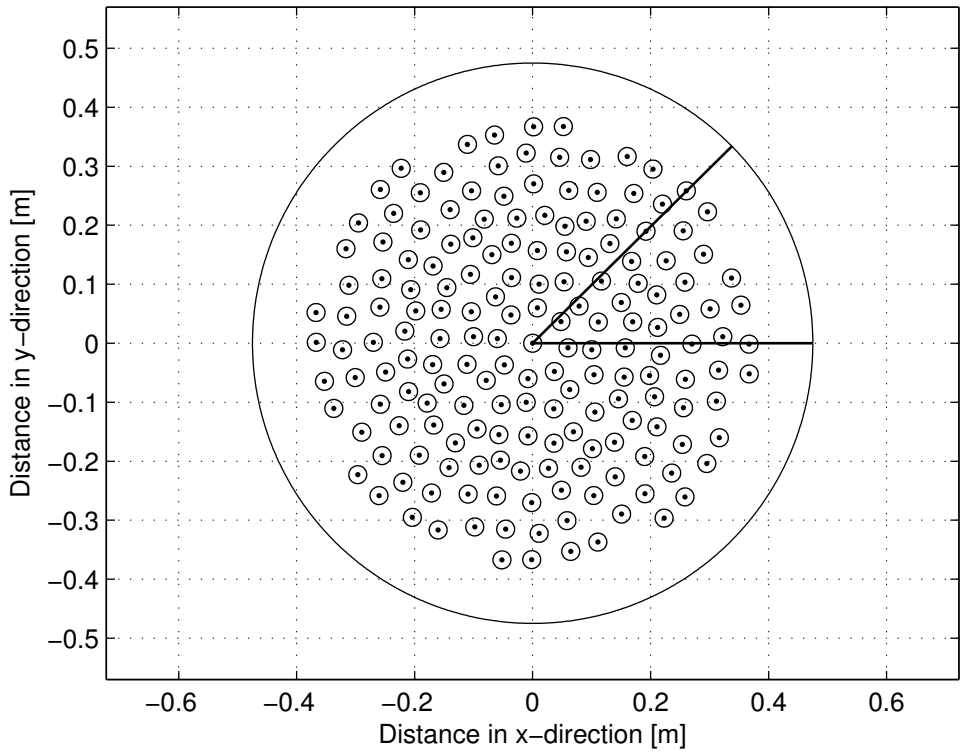

Figure 4.27: Configuration for the large pyramidal horn when it is used to acquire the large spot size of 1°.

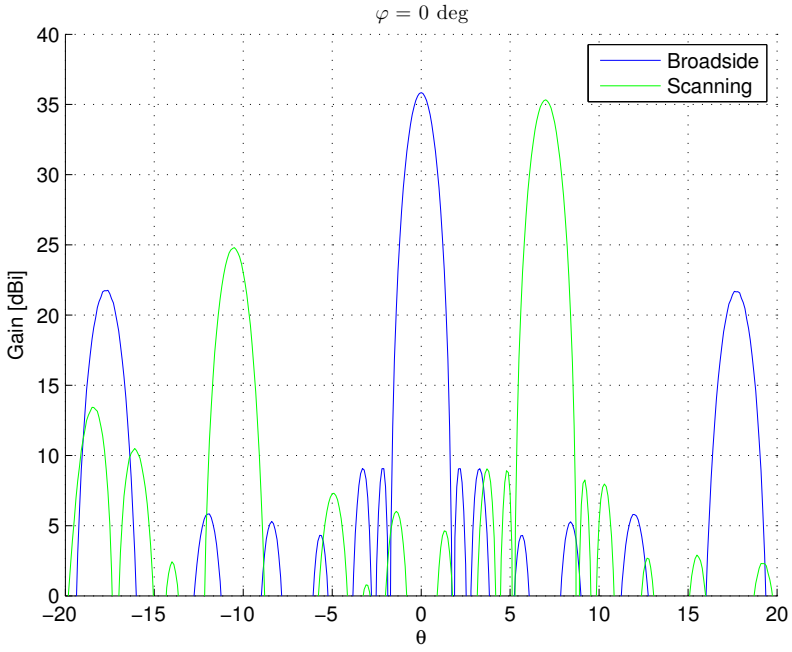

Figure 4.28: For the case of the large pyramidal horn and the large sport size, scanning is shown for the $\varphi = 0°$ plane.

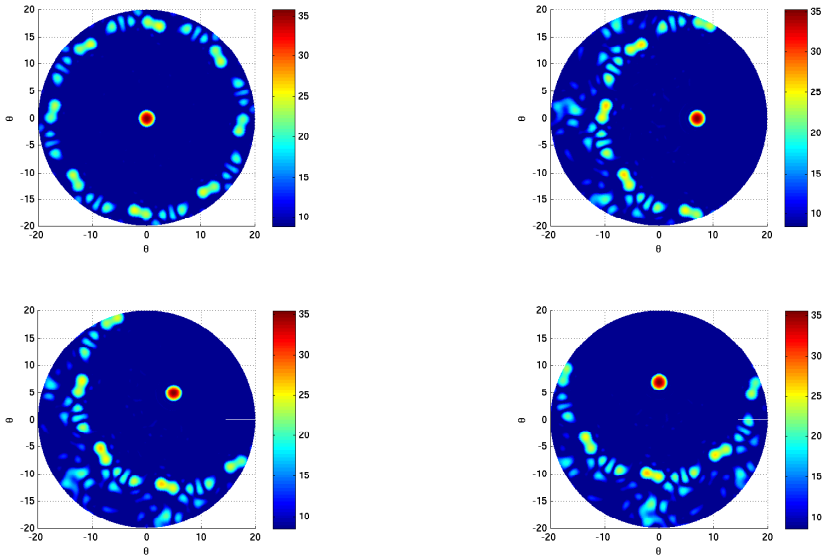

Figure 4.29: Scanning is initiated for the array corresponding to the large pyramidal horn and the large spot size.

4.2.4 Suggested Array Layouts and Their Convergence Behavior

At this point the candidate best suited for a physical demonstrator should be appointed. The candidate that best managed to combine low side-lobes with a low number of elements was the one utilizing the large pyramidal horn element to synthesize the large spot size, the last candidate presented. Furthermore, the arrays synthesized with the large pyramidal horn are those that demonstrate the largest gain, for each respective spot size. No collision occurs for this array candidate. The array elements chosen for convergence testing is shown in Fig. 4.30. The colored marks show which element has given the corresponding curve in Fig. 4.31. The elements are chosen such that both elements close to the center of the array and close to the edge of the array are accounted for.

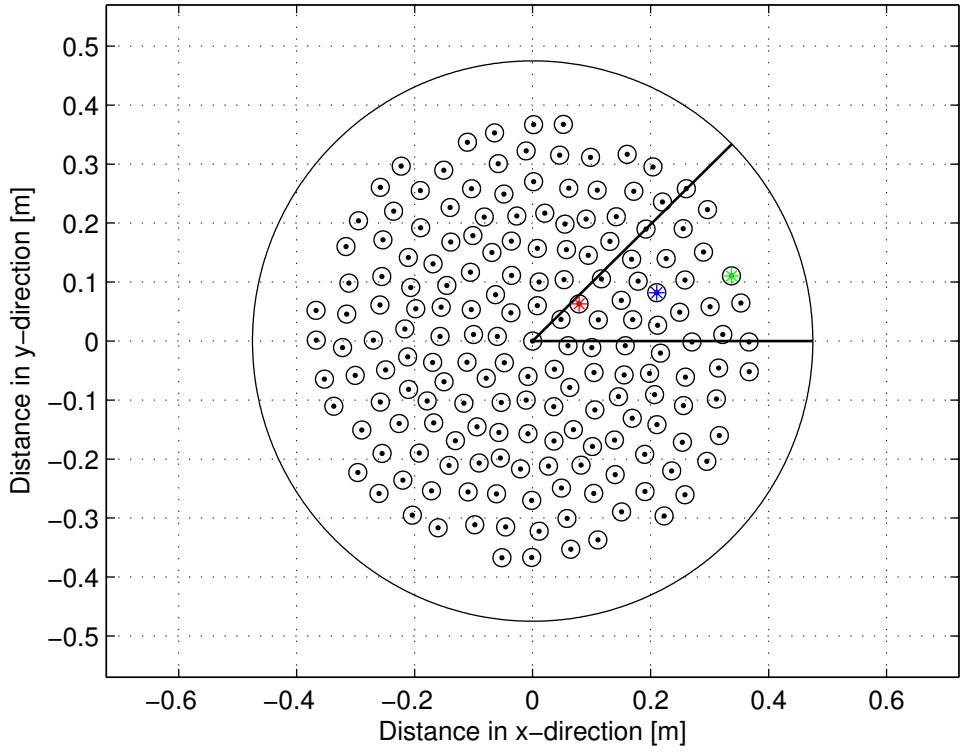

Figure 4.30: Element configuration for the recommended demonstrator layout. The colored markings show which elements has been chosen for convergence testing.

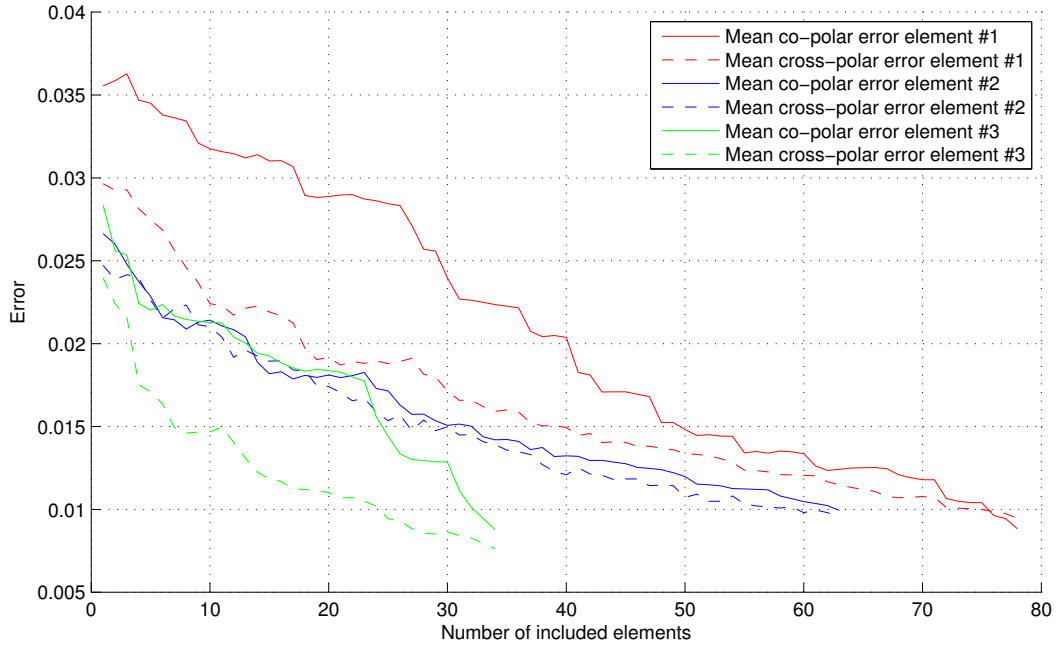

Figure 4.31: Error as a function of included elements for three different elements. The elements belong to the array using the large pyramidal horn to synthesize the large sport size.

4.2.5 Summary on the Array Results

The provided array configurations all adopt eight-fold symmetry in order to synthesize their respective solutions. Also, they are all subject to the same radiation mask constraints; the masks are placed with 5° intervals in φ. The small arrays are suppressing side-lobes in a satisfying way. The large arrays suffer from minor violations to the SLL specification in the spaces between the radiation masks. This only occur for large θ angles, where the distance between the radiation masks is large enough. This might have been mitigated by adding constraints along more φ cuts. Looking at Table 4.1, the highest filling factor is just above 20 %, which is to be considered low. The number of elements utilized is similar for each spot size, although the element configuration is different for each case. The elements are in general evenly distributed across the array aperture, enabling scan in multiple directions.

The recommended candidate is that of the large spot size synthesized with the large pyramidal horn. The convergence is shown for this candidate in Fig. 4.31. It can be seen that, as expected, the convergence is fastest when taking the closest elements into account, and as the local environment grows larger, the EM coupling to the elements further away get smaller and smaller. The convergence algorithm also takes longer time when elements

closer to the center are being evaluated. That is, looking at Fig. 4.31, element number one need to include a larger number of elements than element number three in order to reach convergence. This is since element number one couple more strongly to a larger number of elements on the opposite side of the array. In order to reach error levels below 2 %, 40 elements need to be included. For error levels below 1 %, 77 elements should be included.

Table 4.2: Summary of array layouts for element types and minimization criterions.

Element type	Spot size	# elements	Sparsification factor [%]	Array gain [dBi]
Corrugated Pipe Horn	Small	481	87.48	36.4
	Large	193	79.92	32.1
Small Pyramidal Horn	Small	481	94.16	36.8
	Large	209	89.85	33.1
Large Pyramidal Horn	Small	441	89.68	39.6
	Large	177	83.50	35.8

4.3 Result Discussion

The three array element candidates, which are summarized in Table 4.1, show somewhat different characteristics. The main differences are the element gain and the element aperture size, and these parameters have an immediate impact on array synthesis. The large and small pyramidal horns have the two highest gains and at the same time occupy the smallest area on the array. This is of course an advantage since high gain and small aperture area are both desired traits of an array antenna element, yet they are proportional to one another according to (2.14). This is a typical trade-off; high element gain and simpler underlying feeding network on one side and small, lightweight elements combined with higher placement flexibility on the other. At this point one could define an element aperture efficiency, η_{ap}, as

$$\eta_{\text{ap}} = \frac{A_{\text{eff}}}{A} \times 100\,\% \tag{4.1}$$

where A is the physical aperture area of the element and A_{eff} is the effective aperture area, defined as

$$A_{\text{eff}} = \frac{\lambda^2}{4\pi} G, \tag{4.2}$$

where λ is the wavelength in the surrounding medium and G is the broadside gain of the antenna. Hence,

$$\eta_{\text{ap}} = \frac{\lambda^2}{4\pi} \frac{G}{A} \times 100\,\%. \tag{4.3}$$

Then, according to the data in Table 4.1, we find the η_{ap} for the different array elements which are given in Table 4.3.

Table 4.3: Array antenna element performance measured in effective area over aperture area.

Element	Aperture area [m^2]	Linear gain [-]	η_{ap} [%]
Corrugated Pipe Horn	0.510e-3 [m^2]	7.87	9.89
Small Pyramidal Horn	0.238e-3 [m^2]	11.85	28.94
Large Pyramidal Horn	0.459e-3 [m^2]	22.69	20.71

The values in Table 4.3 give the aperture efficiency of the array elements. Other qualities, such as impedance matching and XPD, are not included in this measure. Hence, it is mostly important from an array synthesis perspective. Note that the corrugated pipe horn has a lower η_{ap} than the pyramidal horns. This is due to the difference in construction technique between the different horns, where the corrugations have been included in the aperture area since they are part of the radiating structure. The large and the small pyramidal horns only differ in flare length, and so η_{ap} is more similar for these array elements. The corrugated pipe horn has the advantage that a physical element already exists. This makes it easier to estimate the behavior of an actual array element, since the simulations will differ somewhat from real measurements. On the other hand, this is the array element with the lowest η_{ap} and the worst XPD, making it a low performing array element compared to the other two.

It is interesting to investigate how the array elements affect the array synthesis process. Looking at Table 4.2, the arrays synthesized using the large pyramidal horn (highest element gain) requires the lowest number of elements. However, the reverse is not strictly true. The arrays synthesized with the corrugated pipe horn (lowest element gain) does not need a larger number of elements than the small pyramidal horn, despite the lower gain for this array element, even though the gain is larger for the arrays synthesized with the small pyramidal horn. If one instead chooses to compare the η_{ap} of the array elements with the filling factor of the different array candidates, one finds that the corrugated pipe horn, which has the lowest η_{ap}, indeed requires the highest filling factor, for both spot sizes. The same goes for the small pyramidal element; it has the highest η_{ap}, which correlates with a lower filling factor for the arrays synthesized with this array element.

According to (2.23), the total gain of an array is approximately the sum of the gains of the individual elements. It can be seen from Table 4.2 that the gain of the complete array configurations increase with the gain of the array element used in a larger extent than with the number of elements included in the array configuration. This is because the effect of a larger array element gain is cumulative with the number of elements in the array configuration. Thus, the best performing array would be that consisting of many elements with large gain. Still, the number of elements needs be minimized, which is the most important aspect of thinned arrays; lesser elements will require a less complex feeding network, so that it will be easier and cheaper to construct, and have smaller losses. The

gains of the individual array elements are for this reason an important parameter that should be maximized. For larger elements the placement flexibility could be so low that the minimization algorithm could not converge, but the array elements presented here are all of such small size that they can be used to find solutions according to the given specifications. As stated in Table 4.2, the filling factor is only around 20 % at most for the array candidates. Antoher impact of the array element type on the results is that larger gain on the array elements lead to larger overall gain of the synthesized arrays. This is why the recommended array candidate can be said to be the most suitable; it manages to combine a low number of elements with high broadside gain and low SLL over the Earth's coverage. It should also be pointed out that the waveguide dimensions for the pyramidal horns do not belong to any standard waveguide dimension. The standard waveguide dimension for the K band is $1.07 \times 0.43\,\text{cm}$ [11]. A physical model of the large or small pyramidal horn may still be employed if done so together with an impedance transformer.

4.3.1 Computational aspects

As the coverage of a future system would be circular, this implies that we need equally good scanning capabilities for all angles of φ. Thus, a typical array would have circular shape since, somewhat simplified, the maximum directivity in a certain φ-plane is proportional to the largest distance between any two elements in that plane. So, the shape of the array is decided by the shape of the coverage area, and the size of the array is decided by the width of the main beam. However, the size of the array aperture will affect other options as well; large array apertures will in general require larger amounts of computer memory in order to be synthesized. This will lead to trade-offs with other parameters such as placement grid resolution, choice of symmetry, and so forth.

Enforcing symmetries in the array element configuration during the array synthesis process is an efficient way of saving memory. The order of symmetry directly affects the number of weights that needs to be included in the complex excitation vector $\mathbf{w}$ by a factor of one over the order of symmetry and will drastically reduce the memory usage. The use of symmetries also reduces the number of constraints in the form of radiation masks that needs to be placed upon the minimization algorithm, which will reduce the required computation time. In fact, including symmetry constraints during the array synthesis is mandatory during the work presented here, since the memory usage is too big otherwise. On the other hand, an order of symmetry that is too high makes thinning of the array inefficient. The candidates presented in Sec. 4.2 are restricted to eight-fold symmetry. This is since this order of symmetry both saved large amounts of memory and at the same time allowed for large placement freedom and relatively low risk of array element collision.

The placement grid resolution also affects the size of the solution set and thus the memory required to synthesize the array. Regarding this parameter, a smaller value implies a

larger flexibility when placing the array elements. In principle, the ideal setting would be to let the grid resolution be as high as possible in order to resemble a continuous, uniform distribution. Since this is impractical, the grid resolution should as high as the system allows for the chosen symmetry. The arrays synthesized here utilizes a grid resolution of $0.2\,\lambda$, which in combination with an eight-fold symmetry results in reasonable computation times.

The use of symmetries and reduction of placement grid resolution both lessen memory usage by reducing the size of the complex excitation vector $\mathbf{w}$, and may impinge on the optimality of the synthesized array solution since there is a possibility that the optimal solution is no longer contained in the solution set. The third improvement of memory usage comes from calculating the far-field for a reduced set of θ angles. Restricting θ to be calculated for a smaller set of angles also saves memory, or, in practice, allows for a finer angular sampling over the area of interest. The specifications for SLL regarding larger angles of θ is self-fulfilling, since the array element gain tapers off for increasing theta angles (see Fig. 4.6, 4.10 and 4.8), and as a consequence, the total array gain does the same. This means that the radiation mask will never, or very seldom, be violated outside of the θ angles for which the array is evaluated.

4.3.2 The Demonstrator Approach

Recalling the convergence algorithm defined in Sec. 3.4, there is a need to assess the minimum number of elements needed in order to construct a physical demonstrator. As more and more elements are included, the embedded field more and more resembles that of the reference solution. The trend is that the first few iterations contribute in a larger amount than later iterations. This is indeed expected, since the EM coupling is stronger for elements close by than for those further apart. The convergence behavior the selected candidate is illustrated in Fig. 4.31.

It is important to assess how well a demonstrator built from the suggestions presented in Sec. 4.2.4 can be expected to work. The approximations made throughout this thesis should not be so crude as to compromise the functionality of a physical demonstrator. The most important approximations are discussed in the following paragraphs.

Upon inspecting Fig. 4.6, we are made aware that the impedance matching between CAESAR and FEKO is not satisfactory in the corrugated pipe horn case. As already mentioned in the same section, this is due to different construction techniques between the software programs. This should not affect the array synthesis process though, since the only thing taken into account when synthesizing arrays are the co-polar pattern of the array element. Since the co-polar patterns match well, and the gain is similar to that calculated when designing the array element at RUAG, the poor impedance matching should not affect the

synthesis of the array.

Regarding the approach of building a physical demonstrator, the pattern convergence has not been checked for all the elements in the recommended candidate. This is simply because the algorithm for pattern convergence control described in Fig. 3.6 requires large amounts of time to converge and controlling all elements is not feasible. However, a representative selection of elements has been selected and controlled. The elements chosen for evaluation can be said to be representative for the whole set of array elements. The trend is also quite clear; the closest elements contribute much more to the embedded pattern than those further away. The large differences in required elements for convergence is due to small contributions to the embedded element pattern.

Chapter 5

Conclusions and Recommendations

5.1 Conclusions

During the element synthesis part of the work, it was discovered that the different full-wave solvers had different approaches to constructing and meshing the array element geometry, which complicated the cross-validation. The array element simulations resulted in three different array element candidates with different gains. These are important in order to assess the impact of the element type in the array synthesis process. The pyramidal horns perform better in terms of η_{ap} and their construction is less complicated. Although some inconsistencies between CAESAR and FEKO persisted for both element types, none of these are believed to affect the array synthesis process.

Several candidates have been evaluated during this work, all with differences in array size or array element type. The available solution set needed to be constrained in order to increase the computational power, which was done by employing an element grid resolution of $0.2\,\lambda$ and eight-fold array symmetry. The resulting candidates all show well-behaving SLL for all φ planes where radiation mask constraints are placed, and only minor violations of the -27 dB level occur inside the region of interest. This is to be expected since the synthesis algorithm removes all redundant elements for fulfilling the radiation masks. The sparsification factor is as large as 79.92–94.16 % which makes these arrays highly suitable.

The arrays synthesized for the small spot size need to utilize their whole array aperture of $100\,\lambda$ in diameter, while the arrays synthesized for the large spot size will in general need less than their appointed aperture, which is $60\,\lambda$ across. The array elements are placed evenly across the apertures of the candidates, which is due to the high number of radiation mask constraints placed on the array synthesis algorithm upon initialization.

A demonstrator constructed from these results can be expected to behave well and it should prove interesting to see what impact the EM coupling would have on the total array far-field function. The number of required elements that needs to be included in order to sufficiently mimic the total solution is around 40 in order to reach error levels below 2 % of broadside levels. This lies above the present goal of 10–15 elements, but is still a reasonable number considering the number of elements in the array.

5.2 Recommendations

It would be interesting to develop a physical demonstrator to further examine the applicability and accuracy of the array synthesis algorithm. The presented candidates can be expected to work well, but scanning is induced via an ideal linear phase shift. Commercial phase shifters are in general restricted to a limited set of beamformer weight levels in order to reduce cost. This effect would be interesting to take into account, both during the array synthesis and scanning of a physical demonstrator.

It is also of interest to include more complex symmetries into the design process. Taking a circular array aperture as an example, perhaps a higher order of symmetry for a larger radius and a lower for a smaller radius would perform better in terms of number of radiating elements, and would probably be more computationally efficient. Including more than one array element type could also be beneficial as suggested in [13].

Appendix A

Blueprint for the pyramidal horns

A blueprint for the pyramidal horns constructed as part of this thesis is provided here. As the horns were simulated, they were situated on an infinite ground plane. Note that the voltage pin thickness, t, extends normal to the paper plane and is not shown in the blueprint. Furthermore, the voltage pin is centered on the waveguide wall.

Measure:	a [mm]	b [mm]	c [mm]	d [mm]	l [mm]	h [mm]	α [rad]	t [mm] (not shown)
Large Pyramidal Horn	19.081734	9.427765	19.786096	21.436745	3.209396	4.048511	0.320114	1.814644
Small Pyramidal Horn	9.540867	9.427765	19.786096	15.432205	3.209396	4.048511	0.320114	1.814644

Appendix B

Position and excitation scheme for the recommended array candidate

Here, the positions and weights of elements utilized in the recommended array candidate is provided. All weights have equal phase since the weights are configurated for broadside scan. The magnitude of the weights are nomalized to the magnitude of the center weight.

Table B.1: Positions and magnitudes for the recommended array candidate.

X	Y	Magnitude	X	Y	Magnitude
0	0	1.0000	-0.0480	-0.0368	0.3892
0.0480	0.0368	0.3892	-0.0787	-0.0630	0.2482
0.0787	0.0630	0.2482	-0.1113	-0.0358	0.3794
0.1113	0.0358	0.3794	-0.1166	-0.1054	0.3999
0.1166	0.1054	0.3999	-0.1502	-0.0691	0.2523
0.1502	0.0691	0.2523	-0.1695	-0.0361	0.2872
0.1695	0.0361	0.2872	-0.1788	-0.1014	0.0911
0.1788	0.1014	0.0911	-0.2120	-0.0268	0.3095
0.2120	0.0268	0.3095	-0.1678	-0.1387	0.2290
0.1678	0.1387	0.2290	-0.2103	-0.0820	0.3223
0.2103	0.0820	0.3223	-0.2492	-0.0488	0.2126
0.2492	0.0488	0.2126	-0.2264	-0.1398	0.3261
0.2264	0.1398	0.3261	-0.1921	-0.1899	0.2489
0.1921	0.1899	0.2489	-0.2582	-0.1035	0.1736
0.2582	0.1035	0.1736	-0.3008	-0.0582	0.1312
0.3008	0.0582	0.1312	-0.2552	-0.1905	0.2206
0.2552	0.1905	0.2206	-0.3223	-0.0111	0.2103
0.3223	0.0111	0.2103	-0.2896	-0.1508	0.3368
0.2896	0.1508	0.3368	-0.3371	-0.1105	0.2124
0.3371	0.1105	0.2124	-0.3529	-0.0646	0.2091
0.3529	0.0646	0.2091	-0.2605	-0.2583	0.0883
0.2605	0.2583	0.0883	-0.2965	-0.2228	0.1203
0.2965	0.2228	0.1203	-0.0079	-0.0600	0.3892
0.0079	0.0600	0.3892	-0.0111	-0.1002	0.2482
0.0111	0.1002	0.2482	-0.0534	-0.1040	0.3794
0.0534	0.1040	0.3794	-0.0079	-0.1570	0.3999
0.0079	0.1570	0.3999	-0.0574	-0.1550	0.2523
0.0574	0.1550	0.2523	-0.0943	-0.1454	0.2872
0.0943	0.1454	0.2872	-0.0547	-0.1982	0.0911
0.0547	0.1982	0.0911	-0.1309	-0.1689	0.3095
0.1309	0.1689	0.3095	-0.0205	-0.2167	0.2290
0.0205	0.2167	0.2290	-0.0908	-0.2067	0.3223
0.0908	0.2067	0.3223	-0.1418	-0.2107	0.2126
0.1418	0.2107	0.2126	-0.0612	-0.2589	0.3261
0.0612	0.2589	0.3261	-0.0016	-0.2701	0.2489

Table B.2: Positions and magnitudes for the recommended array candidate, continued.

X	Y	Magnitude	X	Y	Magnitude
0.0016	0.2701	0.2489	-0.1094	-0.2558	0.1736
0.1094	0.2558	0.1736	-0.1715	-0.2539	0.1312
0.1715	0.2539	0.1312	-0.0458	-0.3152	0.2206
0.0458	0.3152	0.2206	-0.2201	-0.2357	0.2103
0.2201	0.2357	0.2103	-0.0982	-0.3114	0.3368
0.0982	0.3114	0.3368	-0.1602	-0.3165	0.2124
0.1602	0.3165	0.2124	-0.2039	-0.2952	0.2091
0.2039	0.2952	0.2091	-0.0016	-0.3669	0.0883
0.0016	0.3669	0.0883	-0.0521	-0.3672	0.1203
0.0521	0.3672	0.1203	0.0368	-0.0480	0.3892
-0.0368	0.0480	0.3892	0.0630	-0.0787	0.2482
-0.0630	0.0787	0.2482	0.0358	-0.1113	0.3794
-0.0358	0.1113	0.3794	0.1054	-0.1166	0.3999
-0.1054	0.1166	0.3999	0.0691	-0.1502	0.2523
-0.0691	0.1502	0.2523	0.0361	-0.1695	0.2872
-0.0361	0.1695	0.2872	0.1014	-0.1788	0.0911
-0.1014	0.1788	0.0911	0.0268	-0.2120	0.3095
-0.0268	0.2120	0.3095	0.1387	-0.1678	0.2290
-0.1387	0.1678	0.2290	0.0820	-0.2103	0.3223
-0.0820	0.2103	0.3223	0.0488	-0.2492	0.2126
-0.0488	0.2492	0.2126	0.1398	-0.2264	0.3261
-0.1398	0.2264	0.3261	0.1899	-0.1921	0.2489
-0.1899	0.1921	0.2489	0.1035	-0.2582	0.1736
-0.1035	0.2582	0.1736	0.0582	-0.3008	0.1312
-0.0582	0.3008	0.1312	0.1905	-0.2552	0.2206
-0.1905	0.2552	0.2206	0.0111	-0.3223	0.2103
-0.0111	0.3223	0.2103	0.1508	-0.2896	0.3368
-0.1508	0.2896	0.3368	0.1105	-0.3371	0.2124
-0.1105	0.3371	0.2124	0.0646	-0.3529	0.2091
-0.0646	0.3529	0.2091	0.2583	-0.2605	0.0883
-0.2583	0.2605	0.0883	0.2228	-0.2965	0.1203
-0.2228	0.2965	0.1203	0.0600	-0.0079	0.3892
-0.0600	0.0079	0.3892	0.1002	-0.0111	0.2482
-0.1002	0.0111	0.2482	0.1040	-0.0534	0.3794
-0.1040	0.0534	0.3794	0.1570	-0.0079	0.3999
-0.1570	0.0079	0.3999	0.1550	-0.0574	0.2523
-0.1550	0.0574	0.2523	0.1454	-0.0943	0.2872
-0.1454	0.0943	0.2872	0.1982	-0.0547	0.0911
-0.1982	0.0547	0.0911	0.1689	-0.1309	0.3095

Table B.3: Positions and magnitudes for the recommended array candidate, continued.

X	Y	Magnitude	X	Y	Magnitude
-0.1689	0.1309	0.3095	0.2167	-0.0205	0.2290
-0.2167	0.0205	0.2290	0.2067	-0.0908	0.3223
-0.2067	0.0908	0.3223	0.2107	-0.1418	0.2126
-0.2107	0.1418	0.2126	0.2589	-0.0612	0.3261
-0.2589	0.0612	0.3261	0.2701	-0.0016	0.2489
-0.2701	0.0016	0.2489	0.2558	-0.1094	0.1736
-0.2558	0.1094	0.1736	0.2539	-0.1715	0.1312
-0.2539	0.1715	0.1312	0.3152	-0.0458	0.2206
-0.3152	0.0458	0.2206	0.2357	-0.2201	0.2103
-0.2357	0.2201	0.2103	0.3114	-0.0982	0.3368
-0.3114	0.0982	0.3368	0.3165	-0.1602	0.2124
-0.3165	0.1602	0.2124	0.2952	-0.2039	0.2091
-0.2952	0.2039	0.2091	0.3669	-0.0016	0.0883
-0.3669	0.0016	0.0883	0.3672	-0.0521	0.1203
-0.3672	0.0521	0.1203			

Bibliography

[1] R. Maaskant J. Wettergren C. Bencivenni, M. V. Ivashina. Design of maximally sparse antenna arrays in the presence of mutual coupling. *IEEE Antennas and Wireless Propagation Letters*, pages 1–4, 2014.

[2] A. F. Morabito, T. Isernia, M. G. Labate, M. Durso, and O. M. Bucci. Direct radiating arrays for satellite communications via aperiodic tilings. *Progress In Electromagnetics Research*, 93:107–124, 2009.

[3] Y. Cailloce, G. Caille, I. Albert, and J. M. Lopez. A ka-band direct radiating array providing multiple beams for a satellite multimedia mission. pages 403–406, 2000.

[4] C. Mangenot, G. Toso, M. C. Vigano, and A. G. Roederer. Non-periodic direct radiating arrays for multiple beam space telecommunication missions. pages 1–4. IEEE, 2008.

[5] G. Prisco and M. D'Urso. Maximally sparse arrays via sequential convex optimizations. *IEEE Antennas and Wireless Propagation Letters*, 11:192–195, 2012.

[6] ESA/ESTEC. Innovative architectures for reducing the number of controls of multiple beam telecommunication systems. Tender AO/15598/08/NL/ST, Jan. 2008.

[7] C. I. Coman, I. E. Lager, and L. P. Ligthart. Design considerations in sparse array antennas. pages 72–75. IEEE, 2006; 2007.

[8] R. J. Sullivan. *Radar Foundations for Imaging and Advanced Concepts*. SciTech Publishing, Raleigh, NC, 2004.

[9] D. M. Pozar. *Microwave and RF Design of Wireless Systems*. John Wiley and Sons, inc., 2001.

[10] P. Kildal. *Foundations of Antennas - A Unified Approach for Line-Of-Sight and Multipath*. 2014.

[11] D. M. Pozar. *Microwave engineering*. Wiley, Hoboken, NJ, 2012.

[12] R. Maaskant. *Analysis of large antenna systems*. PhD thesis, Eindhoven Univ. of Technology, The Netherlands, 2010.

[13] P. Angeletti, G. Toso, and G. Ruggerini. Array antennas with jointly optimized elements positions and dimensions part ii: Planar circular arrays. *IEEE Transactions on Antennas and Propagation*, 62(4):1627–1639, 2014.